Revealing non-Markovian Kondo transport with waiting time distributions

Feng-Jui Chan [1,2,*] Po-Chen Kuo [2,3,*,†] Neill Lambert [4,‡] Mauro Cirio [5,§] and Yueh-Nan Chen [1,2,6,‖]

[1]*Department of Physics, National Cheng Kung University, Tainan 701, Taiwan*
[2]*Center for Quantum Frontiers of Research and Technology, NCKU, Tainan 701, Taiwan*
[3]*Department of Applied Physics, National Pingtung University, Pingtung 900, Taiwan*
[4]*Theoretical Quantum Physics Laboratory, Cluster for Pioneering Research, RIKEN, Wakoshi, Saitama 351-0198, Japan*
[5]*Graduate School of China Academy of Engineering Physics, Haidian District, Beijing 100193, China*
[6]*Physics Division, National Center for Theoretical Sciences, Taipei 106319, Taiwan*

(Received 3 October 2024; accepted 22 August 2025; published 23 September 2025)

We investigate non-Markovian transport dynamics and signatures of the Kondo effect in a single quantum dot (QD) model. The QD is coupled to a left lead non-Markovian bath and weakly coupled to a right lead, acting as a detector. We calculate the waiting time distribution (WTD) of electrons tunneling into the detector using a combination of the hierarchical equations of motion (HEOM) approach and the Born-Markov (BM) approximation. Oscillations emerge in the short-time WTD, becoming more pronounced with stronger left-lead coupling. Fourier analysis reveals a blueshift in the oscillation frequency as coupling increases, indicating enhanced system-bath hybridization. Crucially, comparison with a master equation confirms that these oscillations are a direct consequence of non-Markovian system-bath correlations. By introducing a toy model, we analyze the role of different parameters, such as coupling strength and bandwidth, in significantly influencing the oscillatory behavior in WTD. In addition, we examine the Kondo effect's influence on these oscillations by varying the coupling strength and the bandwidth of the non-Markovian bath. Decreasing the bandwidth and increasing the coupling strength enhance the WTD oscillations, while also enhancing the Kondo resonance in the quantum dot's density of states. Our results demonstrate that WTD oscillations offer a valuable tool for probing non-Markovian system-bath interactions and the emergence of Kondo correlations within QD systems.

DOI: 10.1103/n4g1-m8s8

I. INTRODUCTION

Open quantum systems, where a system of interest is coupled to one or more environments, exhibit rich dynamics that often deviate from the traditional Markovian picture [1,2]. While many theoretical treatments focus on the wideband limit, studying systems coupled to narrow-band environments is increasingly critical for understanding modern condensed matter platforms, such as Moiré heterostructures and other engineered materials with nearly flat electronic bands [3–7]. These systems are usually strongly coupled to environments characterized by long correlation times, making non-Markovian effects particularly prominent. In the Markovian approximation, the system's evolution is described by a memoryless master equation, such as the Lindblad equation [8–10]. However, this approximation breaks down when the system-environment coupling is strong or when the environmental correlation times become long, leading to non-Markovian dynamics [11–15].

Non-Markovian dynamics are characterized by the backflow of information from the environment to the system, giving rise to memory effects [16–19]. These effects play a crucial role in various quantum processes, including quantum transport in nanoscale devices [20–23]. Understanding and controlling non-Markovian effects is essential for harnessing the full potential of quantum technologies, as they can profoundly impact the coherence and entanglement properties of quantum systems [24–29].

One striking manifestation of strong system-environment coupling is the Kondo effect [30], which arises from the many-body entanglement between electrons in the system and those in the environment [7,31–37]. In particular, QDs have emerged as versatile platforms for engineering and probing the Kondo effect [37–43], offering insights into the interplay between many-body physics and quantum transport [44–48].

A powerful tool for studying the influence of non-Markovian environments and the Kondo effect on quantum transport [37,47–51] is the WTD [52–69], which quantifies the probability density of observing electron transfer events at different time intervals. The WTDs have been extensively used to analyze electron transport in QDs [52–56,68,70–77], revealing coherent oscillations [52,68] and entanglement

*These authors contributed equally to this work.
†Contact author: pochen@mail.nptu.edu.tw
‡Contact author: nwlambert@gmail.com
§Contact author: cirio.mauro@gmail.com
‖Contact author: yuehnan@mail.ncku.edu.tw

signatures [68], and identifying the Majorana states for the Majorana island device [75] and the influence of non-Markovian environments [56]. Importantly, the WTDs can be reconstructed directly from experiments leading to interesting applications such as improving single-electron spin-readout fidelities [71], extracting the short-time scaling of charge fluctuations in parasitic states [72], visualizing the crossover from adiabatic to nonadiabatic dynamics [73], investigating the spin entanglement of split Cooper pairs [74], and analyzing correlated electron transport in nanostructures [77].

Despite advances in understanding non-Markovian transport, its interplay with the Kondo effect in shaping the WTD remains largely unexplored. This work aims to bridge this gap by studying a simple model describing a QD coupled to a (left) non-Markovian lead and weakly coupled to a (right) Markovian lead detector. This allows us to apply the Born-Markov (BM) approximation to the right lead while using the hierarchical equations of motion (HEOM) to model the interaction with the left one nonperturbatively. This approach reveals the emergence of short-time oscillations in the WTD. These oscillations become more pronounced when increasing the left-lead coupling. Fourier analysis reveals that the oscillation frequency shifts due to the enhanced system-environment interactions. We explore this effect using a toy model, which confirms how non-Markovian features, such as a smaller bandwidth and a larger coupling strength, can enhance the amplitude of the oscillations.

Furthermore, we also explore the influence of the Kondo resonance on the WTD by changing the spectral bandwidth and the coupling strength of the left lead. Analyzing the system density of states (DOS), we observe a frequency blueshift and an amplitude increment in the Kondo resonance in correspondence to an increase of the coupling strength. Interestingly, a similar blueshift is accompanied by a lower amplitude of the resonance when it is the bandwidth to be increased. This combined trend, i.e., the enhancement of the WTD oscillations and the amplitude of the Kondo resonance with increasing coupling and decreasing bandwidth, indicates a relationship between the Kondo effect and non-Markovian transport dynamics.

II. WTD REVEALS NON-MARKOVIAN SIGNATURE

As shown in Fig. 1, we consider a QD system coupled to two leads constituting its environment. In the following sections, we analyze the influence of non-Markovianity on the WTD, with an increasing level of complexity for the system, starting with a spinless single-level Anderson model.

A. QD with a single level

For a single-level QD, the total Hamiltonian of the system and leads is ($\hbar = 1$)

$$H_{\mathrm{T}} = H_{\mathrm{s}} + H_{\mathrm{f}} + H_{\mathrm{sf}}, \tag{1}$$

where the QD is described by the system Hamiltonian

$$H_{\mathrm{s}} = \epsilon \hat{n}. \tag{2}$$

Here, $\hat{n} = d^{\dagger}d$ is the number operator and $d^{\dagger}$ is the creation operator for the QD. The leads are described by the

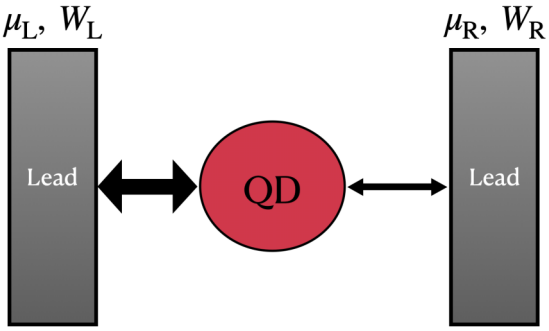

FIG. 1. Schematic representation of the single impurity Anderson model (SIAM) considered in this study. The model depicts a single quantum dot (QD), coupled to a left (non-Markovian) bath (L) and weakly coupled to a right bath (R). The BM approximation is applied to the interaction with the right lead, while the interaction with the left one is treated nonperturbatively. Here, W_{α} and μ_{α} represent the bandwidth and chemical potential of the lead ($\alpha = \mathrm{L}, \mathrm{R}$), respectively.

Hamiltonian

$$H_{\mathrm{f}} = \sum_{k,\alpha} \omega_{k,\alpha} c^{\dagger}_{k,\alpha} c_{k,\alpha}, \tag{3}$$

where $c^{\dagger}_{k,\alpha}$ creates an electron in the state k of the αth lead ($\alpha \in \{\mathrm{L}, \mathrm{R}\}$). The tunneling between the QD and the leads is given by

$$H_{\mathrm{sf}} = \sum_{k,\alpha} g_{k,\alpha}(c^{\dagger}_{k,\alpha} d + d^{\dagger} c_{k,\alpha}), \tag{4}$$

parametrized by the coupling strengths $g_{k,\alpha}$. In the continuum limit, these coefficients can be encoded in a spectral density function for which we choose a Lorentzian line shape

$$J_{\alpha}(\omega) = \frac{\Gamma_{\alpha} W_{\alpha}^2}{(\omega - \mu_{\alpha})^2 + W_{\alpha}^2}. \tag{5}$$

Here, Γ_{α} describes the overall coupling strength between the QD and the α lead, while W_{α} and μ_{α} represent the bandwidth and the chemical potential of the α lead, respectively.

In this work, we assume the interaction between the QD and the left lead to be in a regime that prevents the use of the BM approximation. However, we consider the system to be weakly coupled to the right lead, which allows us to interpret it as a detector with a well-defined WTD. The effects of the fermionic leads on the system are fully encoded in the two-time correlation functions

$$\begin{aligned} C^{\nu}_{\alpha}(t) &= \mathrm{Tr}_{\mathrm{f}}\left[\sum_{k} \Gamma^2_{\alpha,k} c^{\nu}_{k,\alpha} c^{\bar{\nu}}_{k,\alpha} \rho_{\mathrm{f}}(0)\right] e^{\nu i\omega t} \\ &= \frac{1}{2\pi}\int_{-\infty}^{\infty} d\omega J_{\alpha}(\omega)\left[\frac{1-\nu}{2} + \nu n^{\mathrm{eq}}_{\alpha}(\omega)\right] e^{\nu i\omega t}, \end{aligned} \tag{6}$$

in terms of the Fermi-Dirac distribution $n^{\mathrm{eq}}_{\alpha}(\omega) = \{\exp[(\omega - \mu_{\alpha})/k_{\mathrm{B}}T_{\alpha}] + 1\}^{-1}$ at temperature T_{α}, where k_{B} is the Boltzmann constant. Here, $\nu = \pm 1$ characterizes the distinction between particles and holes, and $c^{\nu=1}_{k,\alpha} = c^{\dagger}_{k,\alpha}$ and $c^{\nu=-1}_{k,\alpha} = c_{k,\alpha}$ (with $\bar{\nu} = -\nu$). While the correlations in Eq. (6) cannot in general be written in a closed analytical form, it is usually

advantageous to consider the following ansatz:

$$C_\alpha^\nu(t) = \sum_{l=0}^{l_{\max}} \eta_{\alpha,l}^\nu \exp[-\gamma_{\alpha,\nu,l}(t)]. \tag{7}$$

This representation expresses the correlation as an exponential series, whose strength coefficients $\eta_{\alpha,l}^\nu$ and decay rates $\gamma_{\alpha,\nu,l}$ can be found using the Padé spectral decompositions as in Refs. [78,79].

In order to capture the nonperturbative effects originating from the strong interaction with the left lead, we employ the HEOM approach [79–81], which is, in principle, numerically exact [82] as it goes beyond the standard master equations based on the BM approximation.

This approach enables us to comprehensively explore the interplay between system-bath correlations and non-Markovian transport characteristics. Explicitly, the HEOM for the QD (left lead) system can be written as

$$\partial_t \rho_{\mathbf{j}}^{(m,p)}(t) \equiv \hat{\mathcal{M}} \rho_{\mathbf{j}}^{(m,p)}(t)\,, \tag{8}$$

in terms of the HEOM Liouvillian superoperator $\hat{\mathcal{M}}$, which characterizes the dynamics of the set of auxiliary density operators (ADOs) defined by $\rho_{\mathbf{j}}^{(m,p)}(t)$. Here, the pair (m, p) represents the mth level fermionic ADO with parity p, and $\mathbf{j}$ denotes the vector $[j_m, \ldots, j_1]$, where each j represents a specific ensemble with multiindex $\{\alpha, \upsilon, l, \sigma_{\rm f}\}$ in which $\sigma_{\rm f}$ specifies the remaining system quantum numbers. The parity index $p \in \{+, -\}$ in the fermionic HEOM formulation emerges from the mathematical structure required to fully encode the effects of fermionic anticommutation relations between system and bath operators upon averaging over the environmental degrees of freedom. As a result, all physical density matrices belong to the even-parity sector ($p = +$), while correlation functions for observables like the DOS require the odd-parity sector ($p = -$). Importantly, the even- and odd-parity sectors of the HEOM are independent. This allows each observable to be associated with a HEOM generator having well-defined parity, thereby not requiring a doubling of the computational resources. The superoperator in Eq. (8) can be explicitly defined by its action on the auxiliary density matrices as

$$\begin{aligned}\hat{\mathcal{M}}\rho_{\mathbf{j}}^{(m,p)}(t) = &-\left(i\hat{\mathcal{L}}_{\rm s} + \sum_{w=1}^{m}\gamma_{q_w}\right)\rho_j^{(m,p)}(t)\\ &- i\sum_{j'\notin\mathbf{j}}\hat{\mathcal{A}}_{j'}\rho_{\mathbf{j}^+}^{(m+1,p)}(t)\\ &- i\sum_{w=1}^{m}(-1)^{m-w}\hat{B}_{q_w}\rho_{\mathbf{j}_w}^{(m-1,p)}(t).\end{aligned} \tag{9}$$

Here, $\hat{\mathcal{L}}_{\rm s}[\cdot] = [H_{\rm s}(t), \cdot]$ describes the system dynamics, while $\hat{\mathcal{A}}_j$ and $\hat{\mathcal{B}}_j$ are the fermionic superoperators describing the system-bath interaction. Specifically, they couple the mth-level fermionic ADOs to the $(m+1)$th-level and $(m-1)$th-level fermionic ADOs, and they are explicitly given by

$$\begin{aligned}\hat{\mathcal{A}}_j[\cdot] &= (-1)^{\delta_{p,-}}\left\{d_{\sigma_{\rm f}}^{\bar\upsilon}[\cdot] - \hat{\mathcal{P}}_{\rm s}\left[[\cdot]d_{\sigma_{\rm f}}^{\bar\upsilon}\right]\right\},\\ \hat{\mathcal{B}}_j[\cdot] &= (-1)^{\delta_{p,-}}\left\{\eta_{\alpha,l}^{\upsilon} d_{\sigma_{\rm f}}^{\upsilon}[\cdot] + \left(\eta_{\alpha,l}^{\bar\upsilon}\right)^* \hat{\mathcal{P}}_{\rm s}\left[[\cdot]d_{\sigma_{\rm f}}^{\upsilon}\right]\right\},\end{aligned} \tag{10}$$

in terms of the parity operator $\hat{\mathcal{P}}_{\rm s}$ whose action is defined as

$$\hat{\mathcal{P}}_{\rm s}\left[\rho_{\mathbf{j}}^{(m,\pm)}(t) d_{\sigma_{\rm f}}^{\upsilon}\right] = \mp(-1)^m \rho_{\mathbf{j}}^{(m,\pm)}(t) d_{\sigma_{\rm f}}^{\upsilon}. \tag{11}$$

In contrast, the coupling to the right lead (which will primarily serve as a detector) can be modeled using the typical assumptions valid in the weak coupling regime. This allows for an adequate description of the right-lead influence on the QD using the Born-Markov master equation (BMME).

We include this perturbative treatment for the interaction with the right lead directly into the system Liouvillian by modifying $\hat{\mathcal{L}}_{\rm s}$ to include the Lindblad dissipator

$$\hat{\mathcal{L}}_{\rm s}[\cdot] = [H_{\rm s}(t), \cdot] + \sum_{\upsilon=\pm1} J_{\rm R}(\omega)\left(\frac{1-\upsilon}{2} + \upsilon n_{\rm R}^{\rm eq}(\omega)\right)\hat{\mathcal{D}}^p(d^\upsilon)[\cdot], \tag{12}$$

where $d^{\upsilon=1} = d^\dagger$, $d^{\upsilon=-1} = d$, and $\hat{\mathcal{D}}^p(\hat{O})[\cdot] = p\hat{O}[\cdot]\hat{O}^\dagger - \frac{1}{2}\hat{O}^\dagger\hat{O}[\cdot]$ is the standard Lindblad dissipator (with parity p). As a consequence, the resulting equation of motion incorporates both strong and weak coupling effects. We explicitly note that the dimension of $\hat{\mathcal{M}}$ does not increase with the additional perturbative term modeling the right lead. At the same time, we also note that a negligible difference is found between the results for both the QD's average electron occupation number and the current flowing into the right bath, when computed with this approximated model and the ones computed with a full HEOM simulation for both leads (see Appendix C).

In order to analyze the statistical properties of the electron transport phenomena, the WTD plays a crucial role. In fact, electronic currents are defined by a series of individual electron tunneling events occurring at random time intervals. The WTD quantifies the probability density that an electron transfers to the detector electrode at time $t + \tau$, given that an electron was detected at an earlier time t, and that no electrons were detected in the time interval $[t,\ t + \tau]$. Given its experimental accessibility [71–74,77] and the insight it provides as a potential analytical quantity, we now compute the WTD around the steady state of this model we have described. The WTD in the steady state can be expressed as follows (see the details in Appendix B) [52,60–62,68,75]:

$$\mathcal{W}(\mathcal{J};\tau) = \frac{\mathrm{Tr}[\mathcal{J}e^{\hat{\mathcal{M}}_0\tau}\mathcal{J}\rho_{\rm st}]}{\mathrm{Tr}[\mathcal{J}\rho_{\rm st}]}, \tag{13}$$

where $\rho_{\rm st}$ is the steady state of the ADO space, $\mathcal{J}$ is a superoperator encoding the quantum jumps in the dynamics, and $\hat{\mathcal{M}}_0 = \hat{\mathcal{M}} - \mathcal{J}$ is the superoperator evolving the system in the absence of quantum jumps. Assuming conditions in which the right lead only acts as a sink for electrons, using Eq. (12), the quantum jump operator reads

$$\mathcal{J}\rho_s = \sum_\sigma J_{\rm R}(\omega)\left(1 - n_\alpha^{\rm eq}(\omega)\right) d\rho_s d^\dagger. \tag{14}$$

Since the left lead is allowed to exhibit non-Markovian effects, it is also useful to introduce a measure to quantify the degree of non-Markovianity. In a Markovian process, information flows unidirectionally from the system to the environment, leading to increasingly indistinguishable quantum states over time. Conversely, non-Markovian behavior allows for information to flow back to the system, potentially

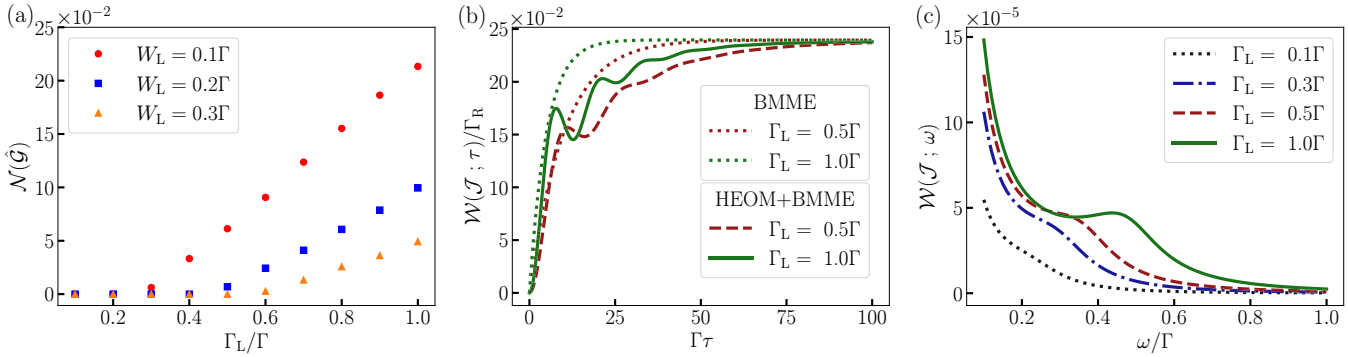

FIG. 2. Non-Markovianity and the WTDs for the open system depicted in Fig. 1. For all panels, the QD's energy is set to $\epsilon = -0.2\Gamma$ in terms of a reference frequency Γ. The bandwidth and the coupling strength for the right lead are $W_R = 5\Gamma$ and $\Gamma_R = 10^{-4}\Gamma$, respectively. In panel (a), we show the non-Markovianity $\mathcal{N}(\hat{\mathcal{G}})$ of the system. $\mathcal{N}(\hat{\mathcal{G}})$ is plotted as a function of the left bath's coupling strength (Γ_L) between the QD and the left lead for different values of left-bath bandwidth W_L. Narrower bandwidths lead to higher non-Markovianity values. In panel (b), we compare the values of the $\mathcal{W}(\mathcal{J};\tau)$ obtained from the HEOM + BMME (solid and dashed lines) and the BMME (dotted lines) for the case $W_L = 0.1\Gamma$. The oscillations emerge in the short-time regime by using HEOM + BMME. In panel (c), we plot the Fourier transform $\mathcal{W}(\mathcal{J};\omega)$ of the WTD as a function of Γ_L by using the HEOM + BMME. The oscillation emerges when $\Gamma_L > 0.3\Gamma$. In addition, the frequency value of the peak blueshifts as the system-bath interaction increases.

overcoming this loss of distinguishability. The trace distance, defined as

$$D(\rho_1, \rho_2) = \tfrac{1}{2}\mathrm{Tr}[\sqrt{(\rho_1 - \rho_2)^\dagger(\rho_1 - \rho_2)}], \tag{15}$$

quantifies the distinguishability between two quantum states ρ_1 and ρ_2. From Eq. (8), the reduced state of the QD system is defined as

$$\rho_s(t) = \rho^{(0,+)}(t) = \hat{\mathcal{G}}(t)[\rho^{(0,+)}(0)], \tag{16}$$

where $\hat{\mathcal{G}}(t) = \exp(\hat{\mathcal{M}}t)$ is the superoperator that propagates all ADOs. For a Markovian process, the distinguishability $D(\rho_{s1}(t), \rho_{s2}(t))$ between two different initial states $s1$ and $s2$ of the QD monotonically decreases over time. However, for non-Markovian systems, a nonmonotonic behavior emerges as a result of information backflow. As a consequence, we can quantify the degree of non-Markovianity by considering the difference in distinguishability with respect to the Markovian case for all possible initial states as

$$\mathcal{N}(\hat{\mathcal{G}}) = \max_{\rho_{s1,s2}(0)} \sum_i [D(\rho_{s1}(b_i), \rho_{s2}(b_i)) - D(\rho_{s1}(a_i), \rho_{s2}(a_i))]. \tag{17}$$

Here, the index i labels the time intervals (a_i, b_i) during which the rate of change of the trace distance is positive, indicating an increase in distinguishability due to non-Markovian information flow [17], i.e.,

$$\frac{d}{dt} D(\rho_{s1}(t), \rho_{s2}(t)) > 0\,, \tag{18}$$

for $t \in (a_i, b_i)$. In the following, we use these technical tools to analyze the electronic transport properties of the model defined in Eq. (1).

In Figs. 2(a) and 2(b), we show the non-Markovianity of the system and the short-time behavior of the $\mathcal{W}(\mathcal{J};\tau)$, where the total system is in equilibrium ($\mu_L = \mu_R = 0$), and the truncation number for the HEOM tiers and the Padé series are $N_H = 4$ and $l_{max} = 3$ (see the details in Appendix D), respectively. To analyze the influence of the system-bath coupling strength on non-Markovianity, we compute the distinguishability of the states during the dynamics. We used Eq. (17) by maximizing all pairs of initial conditions from the set $\{|0\rangle, |1\rangle, \rho_{mix}\}$, where $\rho_{mix} = 1/2(|0\rangle\langle 0| + |1\rangle\langle 1|)$, and $|0\rangle$ ($|1\rangle$) represents the empty (excited) state of the QD.

As expected, the non-Markovian effect becomes increasingly pronounced as the system transitions into the nonperturbative regime. This observation is evident in Fig. 2(a), where stronger Γ_L (ranging from 0.1Γ to 1Γ) leads to an increase in distinguishability. In our observation, this feature is absent when the HEOM is replaced with a BMME to model the strong coupling to the left lead, which demonstrates its inability to capture non-Markovian effects. On the other hand, the result using the HEOM shows that this effect is particularly pronounced when W_L is narrower. This feature can be intuitively justified by considering the Lorentzian shape of the spectral density of the left lead, which corresponds, in this limit, to a correlation that can be written as $C_L^v(t) \propto e^{-W_L t}$ [79,83,84]. As a consequence, a smaller bandwidth W_L corresponds to a slower decay rate, thereby increasing the memory time of the environment.

We now investigate $\mathcal{W}(\mathcal{J};\tau)$ on different values of Γ_L, and compare the results when either the ME or the HEOM is applied to describe the strong interaction with the left lead. A key feature shown in Fig. 2(b) is that oscillations emerge in the WTD only when the HEOM approach is used. Interestingly, the frequency of these oscillations increases with stronger interactions between the QD and the left lead. On the other hand, the full BMME approach fails to reproduce the oscillations shown by the HEOM, which shows that it is not able to correctly model the nonperturbative effects characterizing the coupling to the left lead. Since the HEOM allow modeling all the non-Markovian and nonperturbative effects, these results indicate that a strong lead-system interaction is the cause for the oscillation behavior in $\mathcal{W}(\mathcal{J};\tau)$.

To further describe the oscillatory behavior in $\mathcal{W}(\mathcal{J};\tau)$, we consider its one-sided Fourier transform

$$\mathcal{W}(\mathcal{J};\omega) = \left| \int_0^\infty d\tau e^{i\omega\tau}\, \mathcal{W}(\mathcal{J};\tau) \right| = \left| \frac{\mathrm{Tr}\big[\mathcal{J}(i\omega\mathbb{I} - \hat{\mathcal{M}}_0)^{-1}\mathcal{J}\rho_{\mathrm{st}}\big]}{\mathrm{Tr}[\mathcal{J}\rho_{\mathrm{st}}]} \right|. \tag{19}$$

We analyze this quantity in Fig. 2(c), where we observe an overall shift in the oscillation frequencies as Γ_{L} increases. This indicates the origin of these shifts in the emergence of a stronger system-bath hybridization.

B. Toy model

To provide deeper physical insight into the oscillations observed in the WTD, we introduce a toy model that captures the essential physics while being analytically tractable. We employ the simplest version of the pseudofermion approach [83], in which a single ancillary fermion coupled to a residual bath is used to approximate the effects of the left-lead continuum. Intuitively, this pseudofermion encodes the effects of the collective degrees of freedom in the bath that most strongly interact with the system, thereby modeling the essential system-bath non-Markovian coherent dynamics while making the problem analytically tractable [84]. Specifically, adopting this framework, the left lead is approximated by a pseudofermion coherently coupled to the system, while the right lead remains a weakly coupled detector, as described by the following Hamiltonian:

$$H_{\mathrm{T}}^{\mathrm{t}} = H_{\mathrm{s}}^{\mathrm{t}} + H_{\mathrm{f}}^{\mathrm{t}} + H_{\mathrm{I}}^{\mathrm{t}}. \tag{20}$$

Here, $H_{\mathrm{s}}^{\mathrm{t}}$ characterizes the system QD, $H_{\mathrm{f}}^{\mathrm{t}}$ describes both the pseudofermion (modeling the left lead) and the right lead (acting as a detector), and $H_{\mathrm{I}}^{\mathrm{t}}$ is the interaction Hamiltonian. These Hamiltonians are specifically defined as follows:

$$\begin{aligned} H_{\mathrm{s}}^{\mathrm{t}} &= \epsilon_{\mathrm{s}} d_{\mathrm{s}}^\dagger d_{\mathrm{s}}, \\ H_{\mathrm{f}}^{\mathrm{t}} &= \epsilon_{\mathrm{b}} d_{\mathrm{b}}^\dagger d_{\mathrm{b}} + \sum_{\alpha,k} \omega_k c_{\alpha k}^\dagger c_{\alpha k}, \\ H_{\mathrm{I}}^{\mathrm{t}} &= g_{\mathrm{sb}}(d_{\mathrm{s}}^\dagger d_{\mathrm{b}} + d_{\mathrm{b}}^\dagger d_{\mathrm{s}}) + \sum_k g_{k,\mathrm{L}}(c_{k,\mathrm{L}}^\dagger d_{\mathrm{b}} + d_{\mathrm{b}}^\dagger c_{k,\mathrm{L}}) \\ &\quad + \sum_k g_{k,\mathrm{R}}(c_{k,\mathrm{R}}^\dagger d_{\mathrm{s}} + d_{\mathrm{s}}^\dagger c_{k,\mathrm{R}}), \end{aligned} \tag{21}$$

in terms of the fermionic creation operators for the system $d_{i=\mathrm{s}}^\dagger$, for the pseudofermion $d_{i=\mathrm{b}}^\dagger$, for the electrons in the right lead $c_{k,\mathrm{R}}^\dagger$, and for the pseudofermion's residual bath $c_{k,\mathrm{L}}^\dagger$. Here, g_{sb} is the coherent coupling strength between the system and the pseudofermion. For this model, the equation of motion can be expressed as

$$\begin{aligned} \frac{d\rho(t)}{dt} &= -i\big[H_{\mathrm{s}}^{\mathrm{t}} + g_{\mathrm{sb}}(d_{\mathrm{s}}^\dagger d_{\mathrm{b}} + d_{\mathrm{b}}^\dagger d_{\mathrm{s}}), \rho(t)\big] \\ &\quad + \sum_{\nu=\pm1} 2W_{\mathrm{L}} \hat{\mathcal{D}}\big(d_{\mathrm{b}}^\nu\big)[\rho(t)] \\ &\quad + \sum_{\nu=\pm1} J_{\mathrm{R}}(\epsilon_{\mathrm{s}}) \left(\frac{1-\nu}{2} + \nu n_{\mathrm{R}}^{\mathrm{eq}}(\epsilon_{\mathrm{s}}) \right) \hat{\mathcal{D}}\big(d_{\mathrm{s}}^\nu\big)[\rho(t)] \\ &= \hat{\mathcal{L}}\rho(t). \end{aligned} \tag{22}$$

Here, $g_{\mathrm{sb}} = \sqrt{W_{\mathrm{L}}\Gamma_{\mathrm{L}}/2}$, and $d_i^{-1} = d_i$ and $d_i^{+1} = d_i^\dagger$. Within this framework, we can derive an analytical expression for the WTD by applying Eq. (13) with $\hat{\mathcal{L}}_0 = \hat{\mathcal{L}} - \mathcal{J}$, in terms of the following specific expression for the quantum jump superoperator:

$$\mathcal{J}\rho = J_{\mathrm{R}}(\epsilon_{\mathrm{s}})\big[1 - n_{\mathrm{R}}^{\mathrm{eq}}(\epsilon_{\mathrm{s}})\big] d_{\mathrm{s}} \rho d_{\mathrm{s}}^\dagger. \tag{23}$$

Under the resonant condition $\epsilon_{\mathrm{s}} = \epsilon_{\mathrm{b}}$ and $\mu_{\mathrm{L}} = \mu_{\mathrm{R}} = 0$, our analytical treatment yields the WTD in a compact form as

$$\mathcal{W}(\mathcal{J};\tau) = \sum_{r=\pm} \varepsilon_{ijk}\, c_{i,j,k}^r\, e^{-(A+rq_k)\tau/2}, \tag{24}$$

where ε_{ijk} is the Levi-Civita symbol with implicit summation over repeated indices, and the coefficients $c_{i,j,k}^r$ encode the system parameters [$c_{i,j,k}^\pm = c_{i,j,k}^\pm(W_{\mathrm{L}}, \Gamma_{\mathrm{L}}, \Gamma_{\mathrm{R}}, \epsilon_{\mathrm{s}})$] for appropriate indices (i, j, k) that incorporate sign conventions, with detailed expressions given in Appendix E. The parameter $A = 2W_{\mathrm{L}} + \Gamma_{\mathrm{R}}$ is introduced for notational simplicity.

The oscillatory dynamics are characterized by the terms q_k, which are defined in relation to the roots f_k of a characteristic polynomial:

$$q_k = \sqrt{A^2 + 4f_k}, \quad \text{for } k = 1, 2, 3. \tag{25}$$

These roots f_i are derived from a characteristic cubic polynomial

$$P(z) = 4z^3 + a_2 z^2 + a_1 z + a_0 = 4(z - f_1)(z - f_2)(z - f_3), \tag{26}$$

where $\{f_1, f_2, f_3\}$ are the roots of $P(z) = 0$. The coefficients a_i are functionally dependent on the system parameters [$a_i = a_i(W_{\mathrm{L}}, \Gamma_{\mathrm{L}}, \Gamma_{\mathrm{R}}, \epsilon_{\mathrm{s}})$], with their detailed expressions provided in Appendix E.

To establish the validity and accuracy of this pseudofermion approach, we perform a comprehensive benchmarking analysis against the full HEOM and ME calculations. Figure 3 presents a systematic comparison of the waiting time distributions $\mathcal{W}(\mathcal{J};\tau)$ and their corresponding frequency spectra $\mathcal{W}(\mathcal{J};\omega)$ computed using all three methodological approaches. This validation confirms that our analytically tractable toy model accurately captures the essential non-Markovian features while providing explicit expressions for further theoretical analysis.

The key result from this analysis is that some dynamical features of the WTD can be intuitively understood by interpreting the left lead as acting like a QD. Within this interpretation, the oscillatory behavior of the WTD is a direct consequence of the coherent interaction between the QD and the left lead. Interestingly, this analysis also provides nontrivial quantitative information. In fact, the oscillatory behavior in the WTD emerges when the condition $(2W_{\mathrm{L}} + \Gamma_{\mathrm{R}})^2 + 4f_k < 0$ is satisfied for any of the roots f_k as defined in Eq. (25). Under this condition, q_k becomes purely imaginary, which we can write as $q_k = i\tilde{q}_k$, where $\tilde{q}_k = \sqrt{-[(2W_{\mathrm{L}} + \Gamma_{\mathrm{R}})^2 + 4f_k]}$ is directly related to the WTD oscillation frequencies.

Our analysis reveals two key parameters controlling these oscillations. The first controlling parameter is the coherent coupling strength $g_{\mathrm{sb}} = \sqrt{W_{\mathrm{L}}\Gamma_{\mathrm{L}}/2}$. Increasing this coupling strength makes the roots f_k more negative, thereby increasing the likelihood of satisfying the condition

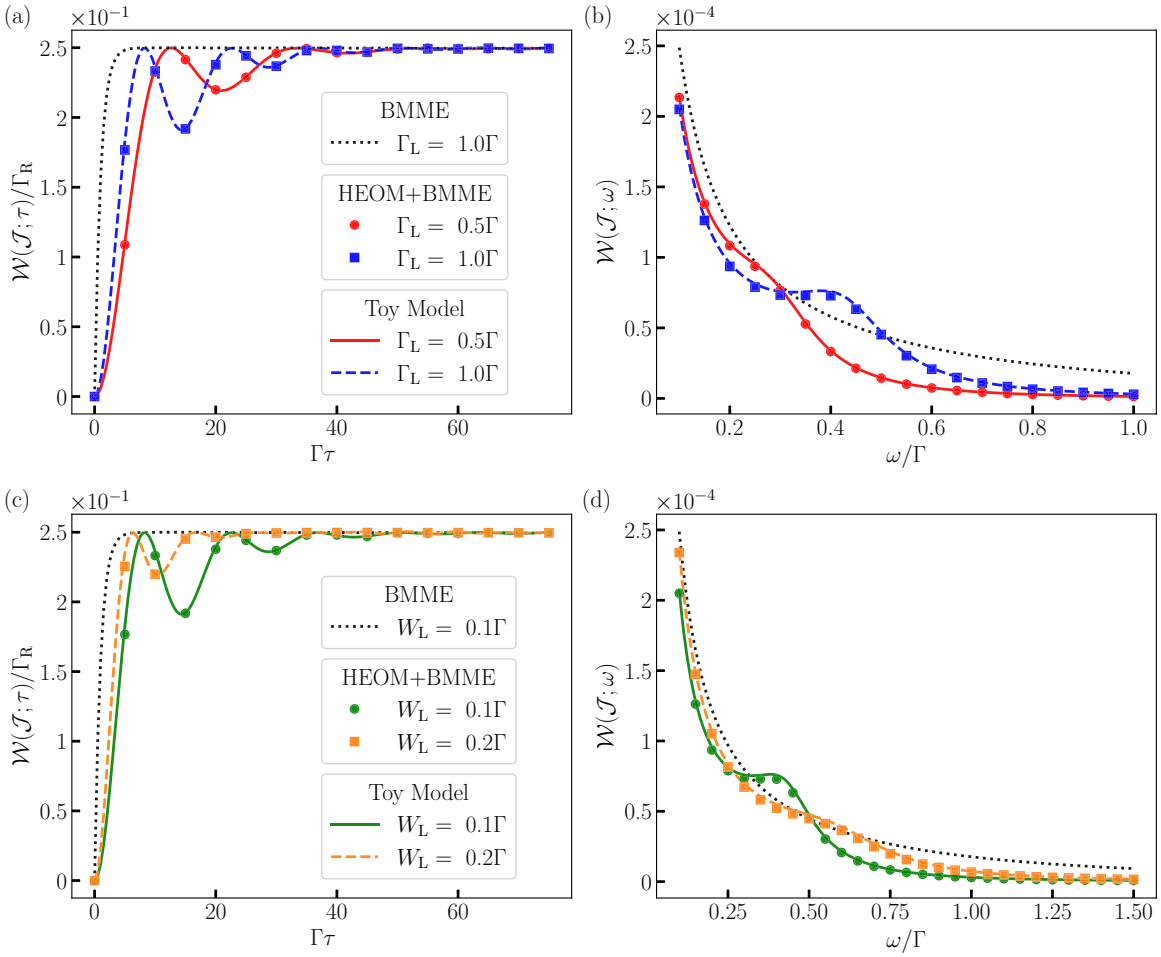

FIG. 3. Oscillatory properties of the WTD in terms of the full and pseudofermion toy model for the case $\epsilon_s = 0$. Other parameters are $\Gamma_R = 10^{-4}\Gamma$, $W_R = 5\Gamma$, and $k_B T_R = 0.5\Gamma$ for all panels. Dotted curves and colored markers represent BMME and HEOM + BMME results, respectively, while colored solid and dot-dashed curves show the pseudofermion toy model predictions. In panels (a) and (b), we plot the WTD in time and frequency domains of the case $W_L = 0.1\Gamma$ for different values of the left-lead coupling strength Γ_L. A stronger system-bath coupling leads to an enhancement of the oscillatory behavior in $\mathcal{W}(\mathcal{J};\tau)$, thereby increasing the characteristic frequency in $\mathcal{W}(\mathcal{J};\omega)$, consistent with the analytical analysis of Eq. (25), where larger Γ_L promotes the oscillatory condition $(2W_L + \Gamma_R)^2 + 4f_k < 0$ through increasingly negative roots f_k. The BMME approach fails to capture these oscillations, confirming their non-Markovian origin. In panels (c) and (d), we plot the WTD in time and frequency domains of the case $\Gamma_L = 1\Gamma$ for different values of the left-lead bandwidth W_L. The enhanced decay triggered by a broader bandwidth suppresses the oscillations in $\mathcal{W}(\mathcal{J};\tau)$, while a narrower bandwidth enhances the oscillation amplitude, leading to more pronounced spectral peaks in $\mathcal{W}(\mathcal{J};\omega)$. The agreement between the toy model and the full numerical results shows the validity of this simplified pseudofermion toy model in capturing the essential non-Markovian features in this specific case.

$(2W_L + \Gamma_R)^2 + 4f_k < 0$ and consequently promoting oscillations. This behavior is clearly demonstrated in Fig. 3(a), where the oscillatory amplitude becomes more pronounced with larger Γ_L.

The second critical parameter is the bandwidth W_L, whose influence is revealed through Eq. (24). This parameter exhibits a dual role: while increasing W_L can increase $\tilde{q}_k$, it simultaneously accelerates the pseudofermion decay rate. This acceleration arises because W_L contributes to the term A, which directly governs the exponential decay as shown in Eq. (24). Consequently, a larger W_L (corresponding to broader bandwidth and shorter memory) suppresses the oscillations in $\mathcal{W}(\mathcal{J};\tau)$. This competing effect is clearly illustrated in Fig. 3(c), where a narrower bandwidth enhances the oscillations in $\mathcal{W}(\mathcal{J};\tau)$.

To highlight the non-Markovian origin of these oscillations, we contrast our results with the Markovian limit, where the WTD reduces to a closed-form expression

$$\mathcal{W}_{\mathrm{ME}}(\mathcal{J};\tau) = \sum_{r=\pm} c_r' e^{-(A'-ru)\tau/2}, \tag{27}$$

where $A' = J_L(\epsilon_s) + J_R(\epsilon_s)$, and the coefficients $c_r' = c_r'(u)$ are detailed in Appendix E. The parameter u is given by

$$u = \Big\{\big(J_L(\epsilon_s) - J_R(\epsilon_s)\big[1 - 2\,n_R^{\mathrm{eq}}(\epsilon_s)\big]\big)^2 + 4\,J_L(\epsilon_s)\,J_R(\epsilon_s)\big[1 - n_L^{\mathrm{eq}}(\epsilon_s)\big]\big[1 - n_R^{\mathrm{eq}}(\epsilon_s)\big]\Big\}^{1/2}, \tag{28}$$

which ensures that $u^2 > 0$ is always satisfied. This mathematical constraint implies that oscillatory behavior cannot emerge

within the Markovian framework, as confirmed by the BMME calculations shown in Figs. 3(a) and 3(c) even when applied to parameter regimes that exhibit strong non-Markovian effects.

To characterize the oscillatory dynamics in frequency space, we analyze the WTD spectrum via Eq. (19). Within the pseudofermion toy model framework (characterized by weak Γ_R and $\epsilon_s = 0$), we derive the analytical solution $\mathcal{W}(\omega)$ with explicit expressions detailed in Appendix E.

The frequency-domain analysis reveals distinct parameter dependencies. As shown in Fig. 3(b), stronger coherent coupling (Γ_L) systematically increases both the amplitude and the peak frequency of $\mathcal{W}(\mathcal{J};\omega)$. Conversely, a larger bandwidth W_L broadens and flattens the spectral peak, while simultaneously shifting its central frequency upward [Fig. 3(d)]. To determine the precise oscillation frequencies ω_{WTD}, we locate the extrema of the spectral magnitude through the condition

$$\frac{d}{d\omega}|\mathcal{W}(\mathcal{J};\omega)||_{\omega=\omega_{\mathrm{WTD}}} = 0\,. \tag{29}$$

The resulting values ω_{WTD} correspond to the peak frequencies in $\mathcal{W}(\mathcal{J};\omega)$, providing direct access to the oscillation frequencies induced by the non-Markovian coupling (Γ_L) and bandwidth (W_L). This provides a quantitative relationship between the system-environment parameters and the resulting transport dynamics. The comprehensive parameter dependence is visualized in Fig. 4, which clearly demonstrates that both larger Γ_L and larger W_L systematically increase the WTD oscillation frequency ω_{WTD}.

Our analysis establishes a clear connection between non-Markovian effects and transport dynamics. Specifically, we identify that a narrower bandwidth (W_L small) and stronger coupling (Γ_L large) both enhance non-Markovian memory effects. This parameter dependence demonstrates that pronounced non-Markovianity correlates directly with the appearance and strength of oscillations in $\mathcal{W}(\mathcal{J};\tau)$. Consequently, these oscillations emerge as a sensitive and quantitative signature of coherent, non-Markovian system-environment correlations within our pseudofermion model framework.

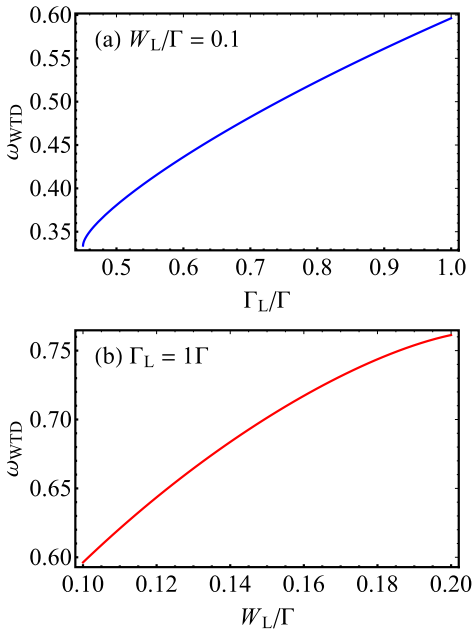

FIG. 4. WTD oscillation frequencies ω_{WTD} as functions of system-environment parameters within the pseudofermion toy model. Frequencies are determined from spectral extrema via Eq. (29). (a) Systematic increase of ω_{WTD} with coupling strength Γ_L/Γ for fixed $W_L/\Gamma = 0.1$, demonstrating that enhanced system-bath coupling elevates oscillation frequency through increasingly negative polynomial roots f_k satisfying the oscillatory condition $(2W_L + \Gamma_R)^2 + 4f_k < 0$. (b) Frequency dependence on bandwidth ratio W_L/Γ_L for fixed $\Gamma_L = 1\Gamma$, revealing that broader environmental bandwidth simultaneously suppresses oscillation amplitude yet increases characteristic frequencies. These parametric relationships provide quantitative mapping between microscopic interaction parameters and observable non-Markovian transport signatures.

III. WTD AND THE KONDO CORRELATION

We now turn to the situation where the QD can be populated with two electrons with spin σ, which interact through a Coulomb repulsion U. This will allow us to see more complex behaviors arising from the nonperturbative system-environment interaction, typified by the well-known Kondo resonance. We start by describing this setup with the SIAM,

$$\begin{aligned} H_s &= \sum_{\sigma=\uparrow,\downarrow} \epsilon \hat{n}_\sigma + U\hat{n}_\downarrow\hat{n}_\uparrow, \\ H_f &= \sum_{k,\alpha,\sigma} \omega_{k,\alpha,\sigma} c^\dagger_{k,\alpha,\sigma} c_{k,\alpha,\sigma}, \\ H_{sf} &= \sum_{k,\alpha,\sigma} g_{k,\alpha} c^\dagger_{k,\alpha,\sigma} d_\sigma + g^*_{k,\alpha} d^\dagger_\sigma c_{k,\alpha}. \end{aligned} \tag{30}$$

Here, $d^\dagger_\sigma$ ($c^\dagger_{k,\alpha,\sigma}$) creates an electron with spin σ in the QD (lead $\alpha \in \{\mathrm{L},\mathrm{R}\}$), and $\hat{n}_\sigma = d^\dagger_\sigma d_\sigma$ describes the number of electrons with σ in the QD. The Coulomb interaction between two electrons has a strength given by the repulsion energy U and is described by the nonlinear operator $\hat{n}_\downarrow\hat{n}_\uparrow$.

When strong system interactions are present, such as those arising from a large Coulomb repulsion U in the QD, the conventional local Lindblad master equation can become unreliable. This unreliability can manifest in unphysical predictions, including excitations at absolute zero temperature [85] or inaccurate electron occupation numbers within the QD. To overcome these problems, it is possible to use a dressed Born-Markov master equation (dBMME), which is more accurate than the conventional local Lindblad master equation [37] to model these regimes. This improvement relies on restricting bath-induced transitions among system eigenstates $|\varphi_i\rangle$ of H_s having energy ϵ_i. Technically, this corresponds to writing the Lindblad dissipator using an eigenbasis decomposition to write Eq. (12) as

$$\left[\sum_{\nu=\pm1}\sum_{\epsilon_k-\epsilon_l=\omega} \gamma^{(\nu)}_{\mathrm{R},l\to k}(\omega)\hat{\mathcal{D}}^p(|\varphi_k\rangle\langle\varphi_l|)\right]\rho^{(m,p)}_{\mathbf{j}(\alpha=\mathrm{R})}, \tag{31}$$

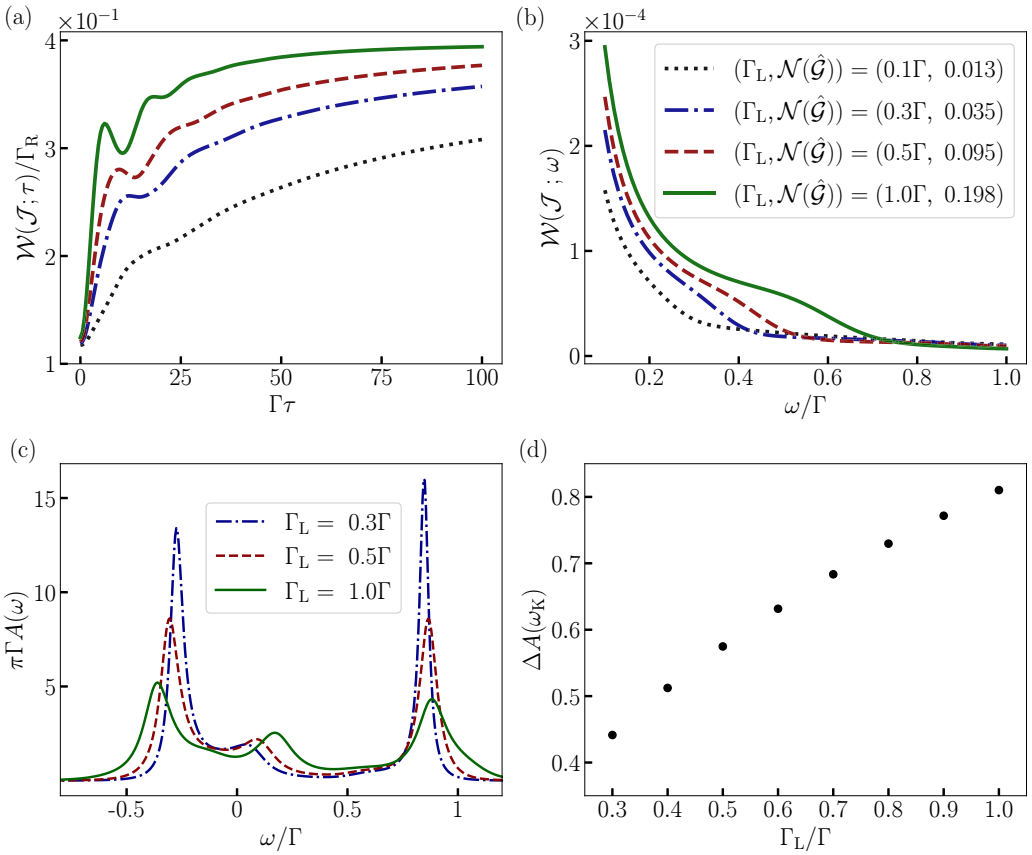

FIG. 5. $\mathcal{W}(\mathcal{J};\tau)$, $\mathcal{W}(\mathcal{J};\omega)$, $A(\omega)$, and $\Delta A(\omega_K)$ for SIAM. Parameters are $\epsilon = -0.2\Gamma$, $\Gamma_R = 10^{-4}\Gamma$, $W_R = 5\Gamma$, $\mu_L = \mu_R = 0$, and $k_B T_R = 0.5\Gamma$. In panels (a) and (b), we plot $\mathcal{W}(\mathcal{J};\tau)$ and $\mathcal{W}(\mathcal{J};\omega)$ for different Γ_L in the case of $k_B T_L = k_B T_R$. Oscillation is more obvious at larger Γ_L, and the oscillation frequency (position of the peak) shifts to a higher value due to the stronger system-bath interaction. In panels (c) and (d), $A(\omega)$ and $\Delta A(\omega_K)$ are depicted as functions of Γ_L. $A(\omega)$ is the spin-up electron DOS. Two Hubbard peaks appear along with a central Kondo peak for $\Gamma_L \geqslant 0.3\Gamma$. The Kondo peak signifies an equilibrium many-body entangled state between the QD and the left lead, and its intensity increases slightly with the larger coupling strength. $\Delta A(\omega_K)$ is the difference in Kondo peak intensity between two temperatures of the left lead, $k_B T_1 = 0.5\Gamma$ and $k_B T_2 = 10\Gamma$, as a measure of Kondo resonance. Larger $\Delta A(\omega_K)$ correlates with stronger coupling and higher-frequency oscillations in $\mathcal{W}(\mathcal{J};\tau)$.

where the transition rates are explicitly given by

$$\gamma^{(\nu)}_{R,l\to k}(\omega) = 2\pi \sum_{\sigma=\uparrow,\downarrow} \left|\langle\varphi_k|d^\nu_\sigma|\varphi_l\rangle\right|^2 J_R(\nu\omega) \times \left(\frac{1-\nu}{2} + \nu n^{eq}_R(\nu\omega)\right). \tag{32}$$

The superoperator for the quantum jumps can now be written in terms of these rates as

$$\mathcal{J}[\rho_s] = \sum_{\epsilon_k-\epsilon_l=\omega} \gamma^{(-1)}_{\alpha,l\to k}(\omega)|\varphi_k\rangle\langle\varphi_l|\rho_s(t)|\varphi_l\rangle\langle\varphi_k|. \tag{33}$$

We are now going to use this formalism in order to analyze the WTD for this open system with a constant on-site Coulomb interaction energy of $U = \Gamma$.

Our analysis reveals that the spin-resolved system exhibits similar behavior to the spinless case examined previously. In Figs. 5(a) and 5(b), we show that the behavior of $\mathcal{W}(\mathcal{J};\tau)$ closely parallels the case without the spin configurations, where the parameters are $W_L = 0.1\Gamma$, $W_R = 5\Gamma$, $\Gamma_R = 10^{-4}\Gamma$, and $k_B T_L = k_B T_R = 0.5\Gamma$. Specifically, both systems demonstrate the same fundamental trend: stronger system-bath coupling (Γ_L) leads to more pronounced oscillations in the WTD.

This similarity extends beyond the WTD behavior to the underlying non-Markovian characteristics. In Fig. 5(b), the non-Markovianity of the system increases due to the large Γ_L. Recall that non-Markovianity is quantified by measuring how much the distinguishability between quantum states can increase over time, as opposed to the monotonic decrease expected in Markovian processes [see Eq. (17)]. When information flows back from the environment to the system, initially different states can become more distinguishable, providing a direct signature of memory effects. For the spin-resolved system, the maximum distinguishability of the two states is calculated from the set composed of the states $\{\rho_k = (1/2)(|\psi_i\rangle\langle\psi_i| + |\psi_j\rangle\langle\psi_j|)\}$, where $(|\psi_{i(j)}\rangle \in \{|0\rangle, |\downarrow\rangle, |\uparrow\rangle, |\downarrow\uparrow\rangle\})$ is the eigenstate of H_s.

The concurrent enhancement of both WTD oscillations and non-Markovianity with increasing Γ_L demonstrates that the oscillations in Figs. 5(a) and 5(b) serve as a reliable signature of non-Markovian system-bath correlations, even when spin degrees of freedom are included. It is important to mention that, here, this behavior is driven by system-bath

interactions rather than the presence of coherent interactions [86,87].

By increasing the rate Γ_L, spin-dependent higher-order tunneling events become more relevant, naturally leading us to consider the relationship between our findings and the Kondo effect. To analyze the interplay between the WTD and Kondo physics, we examine the DOS of the QD, which serves as a fundamental characterization of the electronic behavior and many-body correlations in the system [88]. The DOS quantifies the availability of electronic states at different energies and is mathematically defined as

$$\pi A_\sigma(\omega) = \mathrm{Re}\left\{\int_0^\infty dt\,\langle\{d_\sigma(t), d_\sigma^\dagger(0)\}\rangle e^{i\omega t}\right\}. \tag{34}$$

This expression involves retarded Green's functions with fermionic operator correlations $\langle d_\sigma(t) d_\sigma^\dagger(0)\rangle$, which require the odd-parity sector ($p = -$) in the HEOM formulation due to anticommutation relations, contrasting with transport calculations that use the even-parity sector. The DOS is computed using the parity-dependent HEOM approach [79,89] from Eqs. (8) and (31). Here, $\langle\hat{O}\rangle$ denotes the expectation value of the system operator $\hat{O}$. In the absence of an applied magnetic field, the QD exhibits spin-independent DOS. Therefore, in the following, we will focus on the DOS of the spin-up state, i.e., on the quantity $A(\omega) \equiv A_{\sigma=\uparrow}(\omega)$. For weak system-bath coupling, DOS exhibits two Hubbard peaks located at the resonant energies ϵ and $\epsilon + U$ corresponding to singly and doubly occupied states, respectively. As shown in Fig. 5(c), in the regime where $\Gamma_L \geqslant 0.3\Gamma$, a central Kondo resonance peak appears as a manifestation of the equilibrium many-body entanglement between single-electron states in the system and the electrons in the reservoir continuum. In addition, similarly to the behavior of $\mathcal{W}(\mathcal{J};\omega)$, the Kondo peak also blueshifts as Γ_L increases. Since Kondo correlations are highly temperature-sensitive (thermal fluctuations readily disrupt them [30,90–92]), increasing the lead temperature rapidly suppresses the DOS Kondo peak [37,93–95]. To isolate the true Kondo correlation within the DOS, we examine how the Kondo peak diminishes as the temperature exceeds the Kondo temperature (where the DOS central peak height remains fixed). We compare a lower temperature, $k_B T_1 = 0.5\Gamma$, to a higher one, $k_B T_2 = 10\Gamma$, and calculate the difference in Kondo peak height:

$$\Delta A(\omega_K) = A(\omega_K, T_1) - A(\omega_K, T_2), \tag{35}$$

where ω_K is the Kondo peak frequency. As Γ_L increases, $\Delta A(\omega_K)$ also increases, signifying a stronger Kondo correlation induced by the enhanced QD-lead coupling [see Fig. 5(c)]. In this specific instance, one can quantify the strength of the Kondo correlation from $\Delta A(\omega_K)$. From Figs. 5(a) and 5(d), we observe that larger $\Delta A(\omega_K)$ results in larger WTD oscillation amplitudes. On the other hand, as shown in Figs. 5(b) and 5(d), the frequency ω_K blueshifts for stronger Γ_L. These observations indicate that features of the Kondo resonance are related to the oscillation behavior in $\mathcal{W}(\mathcal{J};\tau)$.

Our study focuses on the "narrow bandwidth" regime ($W_L = 0.1\Gamma$ to 0.5Γ), a choice motivated by both physical relevance and methodological advantages. This regime models contemporary flat-band materials like Moiré heterostructures [3–7]. Methodologically, a narrower bandwidth extends the environmental memory time [$C_L^v(t) \propto e^{-W_L t}$], which amplifies the non-Markovian signatures, as shown in Fig. 2(a). Furthermore, this limit provides a valuable theoretical window into phenomena such as molecular Kondo states [96] and the zero-bandwidth limit of the Anderson model [3,97].

Non-Markovianity can also be used to build a theoretical connection between WTD oscillations and the Kondo effect. In fact, the Kondo effect is itself an inherently non-Markovian process, as the electronic bath must "remember" past spin-flip scattering events to form the characteristic many-body entangled state [98–101]. Since the WTD oscillations also arise from this information backflow, environmental parameters that control memory time should tune both phenomena simultaneously. Consequently, stronger memory effects (narrow bandwidth, and strong coupling) should enhance both phenomena, while weaker memory will cause their simultaneous suppression. Our numerical results in Fig. 6 confirm this connection. There, we investigate the effects of W_L on both the WTD and the Kondo resonance, and find that a wider bandwidth simultaneously suppresses both phenomena.

In Fig. 6(a), we compute $A(\omega)$ for different W_L and the difference $\Delta A(\omega_K)$ between the Kondo peak amplitudes at different temperatures T_1 and T_2 (see the inset). A larger W_L shows a larger ω_K and a smaller $\Delta A(\omega_K)$. This indicates that a narrower bandwidth shifts the ω_K, while increasing the amplitude of the Kondo resonance.

At the same time, as shown in Figs. 6(b) and 6(c), the same increase in W_L decreases both the amplitude and the period of the oscillation in $\mathcal{W}(\mathcal{J};\tau)$. This striking correlation demonstrates that parameters that suppress the Kondo resonance also suppress the WTD oscillations, establishing these oscillations as a sensitive probe of the non-Markovian dynamics that underpin Kondo physics.

IV. CONCLUSIONS

In summary, we have investigated the non-Markovian transport dynamics in a system composed of a QD connected to leads. Specifically, we considered the QD coupled to a non-Markovian (left) lead injecting electrons and weakly coupled to a detector lead. At short times, we observed the emergence of non-Markovianity signatures in terms of oscillations in the WTD (evaluated numerically using the HEOM and a Born-Markov master equation).

As the coupling to the injecting lead is increased, these oscillations become more pronounced and blueshifted in frequency. This effect is due to the hybridization between the system and the left lead, as confirmed by the impossibility to reproduce it using a Markovian master equation.

We further analyzed the influence of different values for the bandwidth of the non-Markovian bath on both the amplitude of the Kondo resonance and the oscillations in the WTD. This sheds light on the relations and influence between non-Markovian system-bath correlations and the properties of the electron WTD and Kondo physics. As an outlook, this work can be generalized by considering the influence of finite voltage biases, and can be extended by calculating the WTD deep in the Kondo regime using fermionic pseudomodes to model strong system-bath interactions [83]. At the same time,

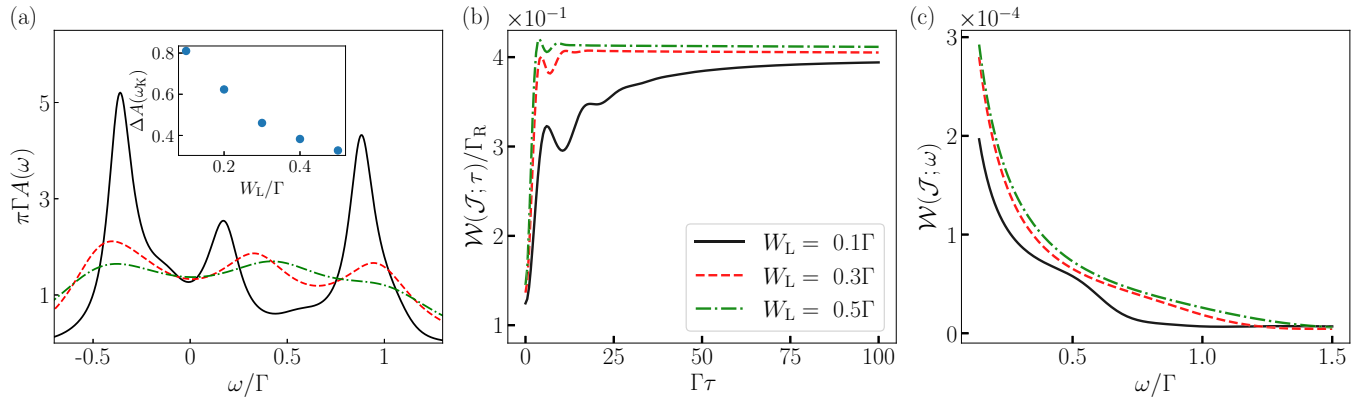

FIG. 6. Numerical analysis of the effect of the left-lead bandwidth W_L on $A(\omega)$, $\mathcal{W}(\mathcal{J};\tau)$, and $\mathcal{W}(\mathcal{J};\omega)$. The black solid, red dashed, and green dash-dotted curves represent the results of $W_L = 0.1\Gamma$, 0.3Γ, and 0.5Γ, respectively. For all panels, $\epsilon = -0.2\Gamma$, $k_B T_L = k_B T_R = 0.5\Gamma$, and $\Gamma_L = 10^4\Gamma_R = 1\Gamma$. In panel (a), we show $\pi A(\omega)$ for different values of the bandwidth W_L of the left lead. For broader values, the Kondo peak amplitude decreases and its frequency shifts. Inset: $\Delta A(\omega_K)$ as a function of W_L. We define $\Delta A(\omega_K)$ as the difference of the Kondo peak between $k_B T_1 = 0.5\Gamma$ and $k_B T_2 = 10\Gamma$. Narrower W_L leads to a stronger Kondo effect. In panels (b) and (c), we analyze the influence of different values for the broadening W_L on $\mathcal{W}(\mathcal{J};\tau)$ and $\mathcal{W}(\mathcal{J};\omega)$. Larger W_L diminishes the amplitude of the oscillations and decreases their period. The peak in $\mathcal{W}(\mathcal{J};\omega)$ disappears for $W_L > 0.3\Gamma$.

an analysis of the full counting statistics [21,64,76,102] using the HEOM could further illuminate the role of non-Markovian effects in electron transport [103].

ACKNOWLEDGMENTS

Y.-N.C. acknowledges the support of the National Center for Theoretical Sciences and the National Science and Technology Council, Taiwan (NSTC Grant No. 114-2112-M-006-015). M.C. acknowledges support from NSFC (Grant No. 12088101) and NSAF (Grant No. U2330401). N.L. was supported by the RIKEN Incentive Research Program and by MEXT KAKENHI (Grants No. JP24H00816 and No. JP24H00820).

DATA AVAILABILITY

The data that support the findings of this study are available from the authors upon reasonable request.

APPENDIX A: DERIVATION AND JUSTIFICATION OF THE HYBRID HEOM-BMME FORMALISM

In this Appendix, we provide a systematic derivation of the hybrid HEOM and BMME approach used in the main text. This addresses the theoretical underpinning of our model, particularly how the influences of a non-Markovian lead and a Markovian lead are combined, and clarifies the physical interpretation of the resulting equations of motion.

1. General propagator formalism for two independent baths

We begin with the total Hamiltonian for a quantum dot (system) coupled to two independent fermionic leads (left and right):

$$H_T = H_s + H_L + H_R + H_{s-L} + H_{s-R}. \tag{A1}$$

After tracing out the lead degrees of freedom, the dynamics of the reduced system density matrix $\rho_s(t)$ can be formally expressed using the Dyson series expansion for the propagator superoperator $\hat{\mathcal{G}}(t)$:

$$\rho_s(t) = \hat{\mathcal{G}}(t)[\rho_s(0)]. \tag{A2}$$

This propagator can be written compactly using the time-ordering operator $\hat{\mathcal{T}}$ and the Feynman-Vernon influence functional $\hat{\mathcal{F}}(t)$:

$$\begin{aligned}\hat{\mathcal{G}}(t)[\cdot] &= \hat{\mathcal{T}}\exp\{-\hat{\mathcal{F}}(t)[\cdot]\} \\ &= \hat{\mathcal{T}}\exp\left\{-\int_0^t dt_1 \int_0^{t_1} dt_2 \hat{\mathcal{W}}(t_1,t_2)[\cdot]\right\}.\end{aligned} \tag{A3}$$

Since the left and right leads are independent, their influences are additive. The total influence functional is the sum of the individual influence functionals:

$$\hat{\mathcal{F}}(t) = \hat{\mathcal{F}}_L(t) + \hat{\mathcal{F}}_R(t). \tag{A4}$$

This separability is the key foundation of our hybrid approach, as it allows us to treat the two leads with different theoretical tools appropriate to their physical characteristics. The superoperator $\hat{\mathcal{W}}(t_1,t_2)$ is consequently also separable: $\hat{\mathcal{W}}(t_1,t_2) = \sum_{\alpha=L,R}\hat{\mathcal{W}}_\alpha(t_1,t_2)$. For the fermionic leads considered in this work, this superoperator takes the form

$$\begin{aligned}\hat{\mathcal{W}}_\alpha(t_1,t_2)[\cdot] = \sum_{p=\pm}\sum_{\sigma}\sum_{\nu=\pm1}\Big\{&C^{\nu}_{\alpha,\sigma}(t_1,t_2)\big[d^{\bar{\nu}}_\sigma(t_2), d^{\nu}_\sigma(t_1)\cdot\big]_{-p} \\ &+ C^{\nu}_{\alpha,\sigma}(t_2,t_1)\big[\cdot d^{\bar{\nu}}_\sigma(t_2), d^{\nu}_\sigma(t_1)\big]_{-p}\Big\}.\end{aligned} \tag{A5}$$

Here, $C^{\nu}_{\alpha,\sigma}(t_1,t_2)$ is the bath correlation function for lead α and spin σ, and $[\cdot,\cdot]_\pm$ are the commutator and anticommutator.

2. Constructing the hybrid equations of motion

Given the separability of the influence functional, we can now formulate a hybrid dynamical generator.

a. Non-Markovian left lead: The HEOM

The left lead is assumed to be strongly coupled to the system, exhibiting non-Markovian memory effects. To handle the time-nonlocal integral involving $\hat{\mathcal{W}}_{\rm L}(t_1,t_2)$, we employ the HEOM method. This is achieved by assuming that the bath correlation function $C^{\nu}_{{\rm L},\sigma}(t)$ can be decomposed into a sum of exponentials, which is a standard procedure. The time differentiation of the propagator then leads to an infinite hierarchy of coupled, time-local linear differential equations for the physical density operator $\rho^{(0)}(t)=\rho_{\rm s}(t)$ and a set of ADOs $\rho^{(\mathbf{n})}(t)$. The generic structure is

$$\partial_t\rho^{(\mathbf{n})}(t)=\Big(-i\hat{\mathcal{L}}_{\rm s}-\sum\gamma_k\Big)\rho^{(\mathbf{n})}(t) + \sum\hat{\mathcal{A}}_{\mathbf{n}'}\rho^{(\mathbf{n}')}(t)+\sum\hat{\mathcal{B}}_{\mathbf{n}''}\rho^{(\mathbf{n}'')}(t), \tag{A6}$$

where $\hat{\mathcal{L}}_{\rm s}[\cdot]=[H_s,\cdot]$, and $\hat{\mathcal{A}}$ and $\hat{\mathcal{B}}$ are superoperators that couple ADOs up and down the hierarchy.

b. Markovian right lead: The BMME and dBMME

The right lead is assumed to be weakly coupled with a very broad bandwidth (short correlation time). This simplifies the bath correlation function to a delta function

$$C^{\nu}_{\rm R}(t_2,t_1)\approx\Gamma_{\rm R}\left(\frac{1-\nu}{2}+\nu n_{\rm R}\right)\delta(t_2-t_1), \tag{A7}$$

where $0\leqslant n_{\rm R}\leqslant 1$. This justifies applying the Born-Markov approximation to its influence functional contribution $\hat{\mathcal{F}}_{\rm R}(t)$. Under this approximation, the time-nonlocal expression collapses into a time-local Lindblad dissipator $\hat{\mathcal{L}}_{\rm R}$:

$$\hat{\mathcal{L}}_{\rm R}[\cdot]=U(t)\frac{d\hat{\mathcal{F}}_{\rm R}(t)}{dt}U(t)[\cdot], \tag{A8}$$

where $U(t)=e^{-iH_st}$. By performing the derivation with the delta-correlated function, we obtain the standard Linblad form as shown in Eq. (12).

We note that this derivation is, in principle, rigorous only in the exact limit when $J_{\rm R}(\omega)\propto\Gamma_{\rm R}$ for all frequencies, and when $n^{\rm eq}_{\rm R}(\omega)$ becomes frequency independent due to infinite bias [104]. Outside this regime, this Lindblad equation can still be used as an approximation, which, within our numerical examples, appears to provide reasonable accurate results.

For the SIAM with strong on-site Coulomb repulsion U, a more accurate form of the Markovian master equation is the dBMME. The dBMME is derived in the eigenbasis [37,83] of the system Hamiltonian H_s, which properly accounts for the system's internal interactions. This leads to the dissipator $\hat{\mathcal{L}}_{\rm dBMME}$ given by Eq. (31).

c. The hybrid HEOM-BMME (dBMME)

Combining these two treatments, the total time evolution of the system is generated by a hybrid Liouvillian. The full equation of motion for the physical density matrix is

$$\partial_t\rho_{\rm s}(t)=(-i\hat{\mathcal{L}}_{\rm s}+\hat{\mathcal{L}}_{\rm BMME\,(dBMME)})\rho_{\rm s}(t) + [\text{HEOM coupling to higher ADOs}]. \tag{A9}$$

When this is expanded into the full hierarchy, the time-local parts of the generator, $-i\hat{\mathcal{L}}_{\rm s}$ and $\hat{\mathcal{L}}_{\rm BMME}$ ($\hat{\mathcal{L}}_{\rm dBMME}$), appear in the evolution of every ADO. The final set of hybrid equations is therefore

$$\partial_t\rho^{(\mathbf{n})}(t)=\Big(-i\hat{\mathcal{L}}_{\rm s}+\hat{\mathcal{L}}_{\rm BMME\,(dBMME)}-\sum\gamma_k\Big)\rho^{(\mathbf{n})}(t) - i\sum_{j'}\hat{\mathcal{A}}_{j'}\rho^{(\mathbf{n}+\mathbf{1})}(t)-i\sum_{w}(-1)^w\hat{\mathcal{B}}_{j_w}\rho^{(\mathbf{n}-\mathbf{1})}(t). \tag{A10}$$

d. Physical interpretation

A key question is how to interpret the BMME (dBMME) dissipator, $\hat{\mathcal{L}}_{\rm BMME}$ ($\hat{\mathcal{L}}_{\rm dBMME}$), which describes the right lead, acting on the ADOs $\rho^{(\mathbf{n})}$ for $\mathbf{n}\neq 0$, since these ADOs encode the memory of the left lead.

The interpretation is twofold:

Formal viewpoint. The HEOM is a mathematical transformation. It replaces the single, complex time-nonlocal equation for $\rho_{\rm s}(t)$ with a larger system of simpler, time-local differential equations. The state of the system is no longer just $\rho_{\rm s}(t)$ but the entire vector of ADOs $\{\rho^{(0)},\rho^{(\mathbf{n}_1)},\rho^{(\mathbf{n}_2)},\dots\}$. The total dynamical generator, which includes the dissipator $\hat{\mathcal{L}}_{\rm BMME}$ ($\hat{\mathcal{L}}_{\rm dBMME}$), acts on this entire extended state space. Thus, from a formal perspective, it is necessary for $\hat{\mathcal{L}}_{\rm dBMME}$ to appear in the equation for every ADO.

Intuitive viewpoint. Each ADO, $\rho^{(\mathbf{n})}(t)$, is an operator that lives in the system's Hilbert space, just like the physical density matrix $\rho_{\rm s}(t)$. An ADO can be physically interpreted as the system's state conditioned on a particular sequence of past interactions with the non-Markovian (left) lead. However, this conditioned state is still a state of the "system," and the system is physically coupled to the right lead. Therefore, the dissipative processes induced by the right lead (e.g., tunneling events) will affect the evolution of the system regardless of its interaction history with the left lead. Since $\hat{\mathcal{L}}_{\rm dBMME}$ describes this dissipation, it must act on any operator representing the system's state, including all ADOs.

In conclusion, our hybrid approach is built on the well-established principle of additive influence functionals for independent baths. This allows for a methodologically sound combination of the HEOM and BMME (dBMME), where the BMME (dBMME) dissipator correctly acts on all operators in the extended HEOM state space, providing a physically and mathematically consistent framework for the problem at hand. Importantly, in constructing the dBMME we neglect hybridization between left lead and system. Our numerical checks demonstrate this induces minimal error for the parameters we employ here. Systematically incorporating the hybridization effect into the dBMME seems challenging, but may be an interesting avenue of future work.

APPENDIX B: WTD FORMULA

The HEOM equation can be expressed as Eq. (8), in terms of a linear kernel that can be written as $\hat{\mathcal{M}}=\hat{\mathcal{M}}_0+\mathcal{J}$. Thus, using this decomposition, the reduced density matrix can be written as

$$\rho^{(0,+)}(t)=e^{\hat{\mathcal{M}}t}\rho^{(0,+)}(0) =\sum_{n=0}^{\infty}\int_0^t dt_n\cdots\int_0^{t_2}dt_1\rho(t|t_1,\dots,t_n), \tag{B1}$$

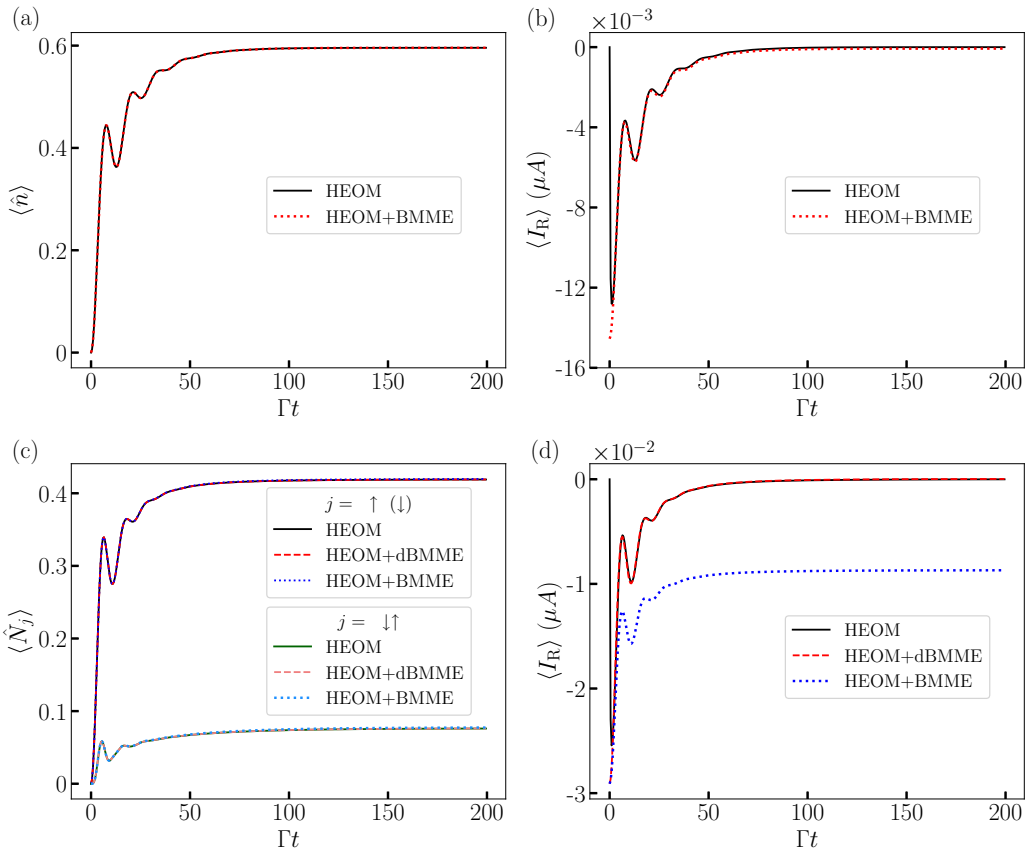

FIG. 7. The particle population, $\langle n \rangle$ ($\langle \hat{N}_j \rangle$), and the transient current from the right bath into the QD, $\langle I_R \rangle$. Parameters are $\epsilon = -0.2\Gamma$, $U = 1\Gamma$, $W_L = 0.1\Gamma$, $\Gamma_L = 1\Gamma$, $W_R = 5\Gamma$, and $\Gamma_R = 10^{-4}\Gamma$. The solid and dotted (dashed) lines represent the results calculated by the full HEOM and hybridization of the HEOM and BMME (dBMME), respectively. In panels (a) and (c), we plot the $\langle \hat{n} \rangle$ ($\langle \hat{N}_j \rangle$) calculated by full HEOM and HEOM + ME (HEOM + dBMME). The results from both methods converge well in panel (a), and the HEOM + dBMME approach shows excellent agreement with the full HEOM in panel (c). In panels (b) and (d), we present the results of the $\langle I_R \rangle$ computed by the full HEOM approach and the hybridized approach. Both methods fit well, except a small deviation in $\langle I_R \rangle$ at $t = 0$ in panel (b). However, panel (d) reveals a substantial deviation when using the HEOM + BMME approach (dotted line) compared to the full HEOM and HEOM + dBMME methods, highlighting the importance of the dressed master equation formalism for accurate current calculations in the presence of strong Coulomb interactions.

with

$$\rho(t|t_n, \ldots, t_1) \equiv e^{\hat{\mathcal{M}}_0(t-t_n)} \mathcal{J} e^{\hat{\mathcal{M}}_0(t_n - t_{n-1})} \mathcal{J} \cdots \mathcal{J} e^{\hat{\mathcal{M}}_0 t_1} \rho_s \tag{B2}$$

being the non-normalized density matrix describing the time evolution of an initial state $\rho_s = \rho^{(0,+)}(0)$, conditioned on n quantum jumps at times t_i ($i = 1, \ldots, n$). For the case of $n = 2$, the quantum jumps happen at t_1 and t_2 so that

$$p_{n=2}(t_2, t_1) = \mathrm{Tr}[\rho(t|t_2, t_1)] \tag{B3}$$

denotes the probability density that two quantum jumps occur at t_1 and t_2, and no quantum jumps in between. The conditional probability density that a particle is emitted at $t_1 = 0$ and the next emission will be at $t_2 = \tau$ can be expressed as

$$P_{n=2}(t_2 - t_1) = \frac{p_{n=2}(t_2, t_1)}{\mathrm{Tr}[\mathcal{J} e^{\hat{\mathcal{M}}_0 t_1} \rho_s]} = \frac{\mathrm{Tr}[\mathcal{J} e^{\hat{\mathcal{M}}_0 \tau} \mathcal{J} \rho_s]}{\mathrm{Tr}[\mathcal{J} \rho_s]}. \tag{B4}$$

This mathematical framework demonstrates that even though we employ the standard WTD formula [Eq. (13)] associated with Markovian quantum jumps, the underlying dynamics $\hat{\mathcal{M}}_0$ contain the full non-Markovian physics from the left-lead interaction.

APPENDIX C: PARTICLE NUMBER AND CURRENT

In this Appendix, we compare the results calculated by the full HEOM and the hybridization of the HEOM and the BMME (dBMME). We show that if the bandwidth and coupling of the right lead are large ($W_R = 5\Gamma$) and weak ($\Gamma_R = 10^{-4}\Gamma$), respectively, the dynamics between the QD and the right lead can be replaced by a BMME (dBMME). We compute the particle occupation in the QD, $\langle \hat{n} \rangle$ ($\langle \hat{N}_j \rangle$), and the current from the QD into the right bath, $\langle I_R \rangle$. The comparison of these two methods is shown in Fig. 7, where the dashed and solid lines represent the full HEOM method and the hybridization of HEOM and BM approximation, respectively.

In Figs. 7(a) and 7(b), we plot the dynamics of $\langle \hat{n} \rangle$ and $\langle I_R \rangle$ in the spinless case using the full HEOM and HEOM + BMME approaches. The compatibility between the

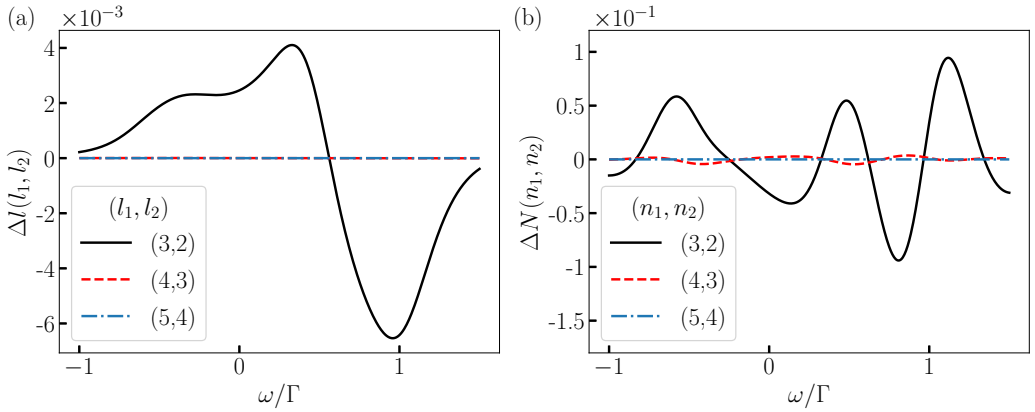

FIG. 8. The difference of DOS obtained by taking two neighboring parameters $\Delta l(l_1, l_2)$, $\Delta N(n_1, n_2)$ in the case of $\epsilon = -0.2\Gamma$, $U = 1\Gamma$, $\mu_L = \mu_R = 0$, $\Gamma_L = 2W_L = 1\Gamma$, $W_R = 5\Gamma$, and $\Gamma_R = 10^{-4}\Gamma$. The black solid, red dashed, and blue dot-dashed lines stand for the two neighboring numbers (3, 2), (4, 3), and (5, 4), respectively. (a) $\Delta l(l_1, l_2)$ computed from Padé number $l = 2$ to $l = 5$. $\Delta l(4, 3)$ and $\Delta l(5, 4)$ indicate that the results are convergent with $l_{max} = 3$. (b) $\Delta N(n_1, n_2)$ calculated from the second-tier hierarchy to the fifth-tier hierarchy. The result is coverage at $N_H = 4$.

full HEOM and HEOM + BMME results indicates that both methods converge well in this regime. We note a discrepancy, limited to very short times, which is due to the capability of the full HEOM method to model higher-order non-Markovian tunneling effects.

In Figs. 7(c) and 7(d), we numerically analyze the dynamics of the quantities $\langle \hat{N}_j \rangle$ and $\langle I_R \rangle$ for the SIAM case using three methods: the full HEOM, HEOM + BMME, and HEOM + dBMME. Here, $\hat{N}_{\downarrow(\uparrow)} = \hat{n}_{\downarrow(\uparrow)}$ and $\hat{N}_{\downarrow\uparrow} = \hat{n}_\downarrow \hat{n}_\uparrow$, respectively. In Fig. 7(c), $\langle \hat{N}_{\downarrow(\uparrow)} \rangle$ ($\langle \hat{N}_{\downarrow\uparrow} \rangle$) the results from the three approaches match well. The results obtained using the HEOM + BMME also match well with those using the full HEOM because U is not large enough to show the advantage of fully nonperturbative methods.

This indicates that dBMME is more accurate than BMME to describe the interaction between the right lead and the QD in the spin-resolved case. Moreover, our hybrid approach maintains fundamental physical consistency, including current conservation. The steady-state current from the left lead into the quantum dot equals the current from the dot into the right lead, as the methodology preserves the continuity equation and probability conservation at the position of the quantum dot. This conservation emerges naturally despite the different theoretical treatments of the two leads.

APPENDIX D: THE CONVERGENCE OF THE DOS

Conventional HEOM studies of Kondo physics typically require numerous Padé poles (8–10 or more) and high tier numbers for convergence, particularly at the low temperatures where Kondo correlations emerge [105]. However, our investigation focuses specifically on narrow bandwidth parameters ($W_L = 0.1\Gamma$ to 0.5Γ), which provide crucial computational advantages. The physical basis for this lies in the fact that narrow bandwidth environments exhibit slower correlation decay rates (proportional to $e^{-W_L t}$), resulting in correlation functions that can be accurately represented with fewer exponential terms in the Padé decomposition. This reduced spectral complexity enables convergent HEOM calculations with significantly fewer Padé poles while preserving the essential non-Markovian physics central to our investigation.

To rigorously verify our convergence parameters under these conditions, we examined the difference in density of states between neighboring Padé pole numbers: $\Delta l(l_1, l_2)$ at the fourth-tier hierarchy level. As shown in Fig. 8(a), the convergence of $\Delta l(4, 3)$ and $\Delta l(5, 4)$ confirms truncation at $l_{max} = 3$. Additionally, we validated the tier convergence by computing $\Delta N(n_1, n_2)$, the difference in DOS between n_1-tier and n_2-tier calculations with $l_{max} = 3$. The negligible values of $\Delta N(4, 3)$ and $\Delta N(5, 4)$ in Fig. 8(b) demonstrate convergence at $N_H = 4$ tiers. Our parameter regime, while enabling computational tractability, captures the essential Kondo physics as evidenced by the characteristic three-peak structure in the density of states and the temperature-dependent Kondo resonance behavior shown in the main text.

APPENDIX E: PSEUDOFERMION TOY MODEL: MATHEMATICAL FORMULATIONS

This Appendix provides the detailed mathematical expressions for the pseudofermion toy model introduced in Sec. II B. We present the complete analytical formulations for the waiting time distribution, characteristic polynomial coefficients, and frequency-domain analysis.

1. WTD for the toy model: Detailed coefficients

Under the resonant condition $\epsilon_s = \epsilon_b$ and $\mu_L = \mu_R = 0$, the WTD from Eq. (24) takes the explicit form

$$\mathcal{W}(\mathcal{J}; \tau) = \sum_{r=\pm} \varepsilon_{ijk}\, c^r_{i,j,k}\, e^{-(A + r q_k)\tau/2}, \tag{E1}$$

where the coefficients $c^r_{i,j,k}$ are given by

$$c^r_{i,j,k} = \frac{-W_L^2 \Gamma_L \Gamma_R}{4A} \frac{q_j q_k (f_j - f_k)\, r X_i^r}{\prod_{1 \leqslant i < j \leqslant 3} (f_i - f_j) \prod_{k=1}^{3} q_k}. \tag{E2}$$

The auxiliary functions $X_k^\pm$ are defined as

$$X_k^\pm = A(A^2 + 4f_k) \mp q_k (A^2 + 2f_k), \tag{E3}$$

with the notation $A = 2W_L + \Gamma_R$ for simplicity.

2. Characteristic polynomial and root structure

The oscillatory dynamics are governed by the roots $\{f_1, f_2, f_3\}$ of the characteristic cubic polynomial

$$P(z) = 4z^3 + a_2 z^2 + a_1 z + a_0 = 4(z - f_1)(z - f_2)(z - f_3). \tag{E4}$$

The coefficients a_i depend explicitly on the system parameters $(W_L, \Gamma_L, \Gamma_R, \epsilon_s)$ and are given by

$$a_0 = 2W_L^2 \Gamma_L \Gamma_R (2W_L + \Gamma_R)^2, \tag{E5}$$

$$a_1 = 2W_L\big[4W_L^2(\Gamma_L + \Gamma_R) + 4W_L\Gamma_R(2\Gamma_L + \Gamma_R) + \Gamma_R\big(\Gamma_R(\Gamma_L + \Gamma_R) + 4\epsilon_s^2\big)\big], \tag{E6}$$

$$a_2 = 4W_L(W_L + 2\Gamma_L) + 12W_L\Gamma_R + \Gamma_R^2 + 4\epsilon_s^2. \tag{E7}$$

The oscillatory condition $(2W_L + \Gamma_R)^2 + 4f_k < 0$ for any root f_k determines when the system exhibits non-Markovian oscillatory behavior.

3. Markovian limit: Analytical benchmark

For comparison with the non-Markovian results, the Markovian limit yields the closed-form waiting time distribution:

$$\mathcal{W}_{\mathrm{ME}}(\mathcal{J};\tau) = \sum_{r=\pm} c_r' e^{-(A' - ru)\tau/2}, \tag{E8}$$

where $A' = J_L(\epsilon_s) + J_R(\epsilon_s)$, and the coefficients are

$$c_r' = \frac{J_R(\epsilon_s)}{u}\left[1 - n_R^{\mathrm{eq}}(\epsilon_s)\right]\left[J_L(\epsilon_s)\, n_L^{\mathrm{eq}}(\epsilon_s) + J_R(\epsilon_s)\, n_R^{\mathrm{eq}}(\epsilon_s)\right]. \tag{E9}$$

The parameter u is defined as

$$u = \Big\{\big(J_L(\epsilon_s) - J_R(\epsilon_s)\left[1 - 2\, n_R^{\mathrm{eq}}(\epsilon_s)\right]\big)^2 + 4\, J_L(\epsilon_s)\, J_R(\epsilon_s)\left[1 - n_L^{\mathrm{eq}}(\epsilon_s)\right]\left[1 - n_R^{\mathrm{eq}}(\epsilon_s)\right]\Big\}^{1/2}, \tag{E10}$$

which ensures $u^2 > 0$, precluding oscillatory behavior in the Markovian framework.

4. Frequency-domain analysis

In the frequency domain, the pseudofermion toy model (for weak Γ_R and $\epsilon_s = 0$) yields the analytical spectrum

$$\mathcal{W}(\mathcal{J};\omega) \approx \left| \frac{W_L\, \Gamma_L\, \Gamma_R\, B(\omega)\, [B(\omega)C(\omega)]}{2\omega\big\{B(\omega)^2[\omega^2 - 2\, W_L\, (\Gamma_L + i\omega)]\big\}} \right|, \tag{E11}$$

where the auxiliary functions are defined as

$$B(\omega) = i(\omega - iW_L), \tag{E12}$$

$$C(\omega) = \omega - 2iW_L. \tag{E13}$$

The precise oscillation frequencies ω_{WTD} are determined by locating the extrema of the spectral magnitude:

$$\frac{d}{d\omega}|\mathcal{W}(\mathcal{J};\omega)||_{\omega=\omega_{\mathrm{WTD}}} = 0. \tag{E14}$$

This condition leads to the characteristic equation

$$3\omega^8 + 2W_L(13W_L - 8\Gamma_L)\omega^6 + 8W_L^2\big(8W_L^2 - 13W_L\Gamma_L + 2\Gamma_L^2\big)\omega^4 + 32W_L^4\big(W_L^2 - 2W_L\Gamma_L + 4\Gamma_L^2\big)\omega^2 + 64W_L^6\,\Gamma_L^2 = 0. \tag{E15}$$

The real parts of the roots of this equation correspond to the peak frequencies $\mathrm{Re}[\omega] = \omega_{\mathrm{WTD}}$ in $\mathcal{W}(\mathcal{J};\omega)$, providing direct access to the oscillation frequencies induced by the non-Markovian coupling strength (Γ_L) and environmental bandwidth (W_L). These analytical results establish the pseudofermion approach as a powerful framework for understanding non-Markovian quantum transport phenomena while maintaining computational tractability.

[1] H.-P. Breuer and F. Petruccione, *The Theory of Open Quantum Systems* (Oxford University Press, New York, 2002).

[2] D. Manzano, A short introduction to the Lindblad master equation, AIP Adv. **10**, 025106 (2020).

[3] S. Schäfer, Anderson impurity model with a narrow-band host: From orbital physics to the Kondo effect, Phys. Rev. B **83**, 195110 (2011).

[4] R. Allub and C. R. Proetto, Hybrid quantum dot–superconducting systems: Josephson current and Kondo effect in the narrow-band limit, Phys. Rev. B **91**, 045442 (2015).

[5] S. Shen, C. Wen, P. Kong, J. Gao, J. Si, X. Luo, W. Lu, Y. Sun, G. Chen, and S. Yan, Inducing and tuning Kondo screening in a narrow-electronic-band system, Nat. Commun. **13**, 2156 (2022).

[6] C. Kourris and M. Vojta, Kondo screening and coherence in kagome local-moment metals: Energy scales of heavy fermions in the presence of flat bands, Phys. Rev. B **108**, 235106 (2023).

[7] N. H. Tu, D. Kim, M. L. Kim, J. Shim, R. Ito, D. Pomaranski, I. V. Borzenets, A. Ludwig, A. D. Wieck, H.-S. Sim, and M. Yamamoto, Electrical control of a Kondo spin screening cloud, arXiv:2404.11955.

[8] E. Davies, *Quantum Theory of Open Systems* (Academic Press, London, 1976).

[9] H. Carmichael, *An Open Systems Approach to Quantum Optics* (Springer, Berlin, 1991).

[10] H.-P. Breuer and F. Petruccione, *The Theory of Open Quantum Systems* (Oxford University Press, New York, 2007).

[11] B.-H. Liu, L. Li, Y.-F. Huang, C.-F. Li, G.-C. Guo, E.-M. Laine, H.-P. Breuer, and J. Piilo, Experimental control of the transition from Markovian to non-Markovian dynamics of open quantum systems, Nat. Phys. **7**, 931 (2011).

[12] W.-M. Zhang, P.-Y. Lo, H.-N. Xiong, M. W.-Y. Tu, and F. Nori, General non-Markovian dynamics of open quantum systems, Phys. Rev. Lett. **109**, 170402 (2012).

[13] H.-N. Xiong, P.-Y. Lo, W.-M. Zhang, D. H. Feng, and F. Nori, Non-Markovian complexity in the quantum-to-classical transition, Sci. Rep. **5**, 13353 (2015).

[14] H.-P. Breuer, E.-M. Laine, J. Piilo, and B. Vacchini, *Colloquium*: Non-Markovian dynamics in open quantum systems, Rev. Mod. Phys. **88**, 021002 (2016).

[15] I. de Vega and D. Alonso, Dynamics of non-Markovian open quantum systems, Rev. Mod. Phys. **89**, 015001 (2017).

[16] M. M. Wolf, J. Eisert, T. S. Cubitt, and J. I. Cirac, Assessing non-Markovian quantum dynamics, Phys. Rev. Lett. **101**, 150402 (2008).

[17] H.-P. Breuer, E.-M. Laine, and J. Piilo, Measure for the degree of non-Markovian behavior of quantum processes in open systems, Phys. Rev. Lett. **103**, 210401 (2009).

[18] E.-M. Laine, J. Piilo, and H.-P. Breuer, Measure for the non-Markovianity of quantum processes, Phys. Rev. A **81**, 062115 (2010).

[19] F. Liu, X. Zhou, and Z.-W. Zhou, Memory effect and non-Markovian dynamics in an open quantum system, Phys. Rev. A **99**, 052119 (2019).

[20] A. Braggio, J. König, and R. Fazio, Full counting statistics in strongly interacting systems: Non-Markovian effects, Phys. Rev. Lett. **96**, 026805 (2006).

[21] C. Flindt, T. Novotný, A. Braggio, M. Sassetti, and A.-P. Jauho, Counting statistics of non-Markovian quantum stochastic processes, Phys. Rev. Lett. **100**, 150601 (2008).

[22] G. Schaller, G. Kießlich, and T. Brandes, Transport statistics of interacting double dot systems: Coherent and non-Markovian effects, Phys. Rev. B **80**, 245107 (2009).

[23] S. V. Moreira, B. Marques, R. R. Paiva, L. S. Cruz, D. O. Soares-Pinto, and F. L. Semião, Enhancing quantum transport efficiency by tuning non-Markovian dephasing, Phys. Rev. A **101**, 012123 (2020).

[24] B. Bellomo, R. Lo Franco, and G. Compagno, Non-Markovian effects on the dynamics of entanglement, Phys. Rev. Lett. **99**, 160502 (2007).

[25] A. Rivas, S. F. Huelga, and M. B. Plenio, Entanglement and non-Markovianity of quantum evolutions, Phys. Rev. Lett. **105**, 050403 (2010).

[26] S. Cialdi, D. Brivio, E. Tesio, and M. G. A. Paris, Programmable entanglement oscillations in a non-Markovian channel, Phys. Rev. A **83**, 042308 (2011).

[27] S. F. Huelga, A. Rivas, and M. B. Plenio, Non-Markovianity-assisted steady state entanglement, Phys. Rev. Lett. **108**, 160402 (2012).

[28] J.-S. Xu, K. Sun, C.-F. Li, X.-Y. Xu, G.-C. Guo, E. Andersson, and R. L. Franco, Experimental recovery of quantum correlations in absence of system-environment back-action, Nat. Commun. **4**, 2851 (2013).

[29] A. Orieux, A. D'Arrigo, G. Ferranti, R. L. Franco, G. Benenti, E. Paladino, G. Falci, F. Sciarrino, and P. Mataloni, Experimental on-demand recovery of entanglement by local operations within non-Markovian dynamics, Sci. Rep. **5**, 8575 (2015).

[30] L. Kouwenhoven and L. Glazman, Revival of the Kondo effect, Phys. World **14**, 33 (2001).

[31] S. Y. Cho and R. H. McKenzie, Quantum entanglement in the two-impurity Kondo model, Phys. Rev. A **73**, 012109 (2006).

[32] L. Amico, R. Fazio, A. Osterloh, and V. Vedral, Entanglement in many-body systems, Rev. Mod. Phys. **80**, 517 (2008).

[33] I. Affleck, N. Laflorencie, and E. S. Sørensen, Entanglement entropy in quantum impurity systems and systems with boundaries, J. Phys. A: Math. Theor. **42**, 504009 (2009).

[34] S.-S. B. Lee, J. Park, and H.-S. Sim, Macroscopic quantum entanglement of a Kondo cloud at finite temperature, Phys. Rev. Lett. **114**, 057203 (2015).

[35] C. Wagner, T. Chowdhury, J. H. Pixley, and K. Ingersent, Long-range entanglement near a Kondo-destruction quantum critical point, Phys. Rev. Lett. **121**, 147602 (2018).

[36] D. Kim, J. Shim, and H.-S. Sim, Universal thermal entanglement of multichannel Kondo effects, Phys. Rev. Lett. **127**, 226801 (2021).

[37] P.-C. Kuo, N. Lambert, M. Cirio, Y.-T. Huang, F. Nori, and Y.-N. Chen, Kondo QED: The Kondo effect and photon trapping in a two-impurity Anderson model ultrastrongly coupled to light, Phys. Rev. Res. **5**, 043177 (2023).

[38] D. Sprinzak, Y. Ji, M. Heiblum, D. Mahalu, and H. Shtrikman, Charge distribution in a Kondo-correlated quantum dot, Phys. Rev. Lett. **88**, 176805 (2002).

[39] M. Avinun-Kalish, M. Heiblum, A. Silva, D. Mahalu, and V. Umansky, Controlled dephasing of a quantum dot in the Kondo regime, Phys. Rev. Lett. **92**, 156801 (2004).

[40] M. Pustilnik and L. Glazman, Kondo effect in quantum dots, J. Phys.: Condens. Matter **16**, R513 (2004).

[41] A. J. Keller, S. Amasha, I. Weymann, C. P. Moca, I. G. Rau, J. A. Katine, H. Shtrikman, G. Zaránd, and D. Goldhaber-Gordon, Emergent SU(4) Kondo physics in a spin–charge-entangled double quantum dot, Nat. Phys. **10**, 145 (2014).

[42] K. Le Hur, Quantum dots and the Kondo effect, Nature (London) **526**, 203 (2015).

[43] R.-N. Shang, T. Zhang, G. Cao, H.-O. Li, M. Xiao, G.-C. Guo, and G.-P. Guo, Direct observation of the orbital spin Kondo effect in gallium arsenide quantum dots, Phys. Rev. B **97**, 085307 (2018).

[44] H. Jeong, A. M. Chang, and M. R. Melloch, The Kondo effect in an artificial quantum dot molecule, Science **293**, 2221 (2001).

[45] A. Komnik and A. O. Gogolin, Full counting statistics for the Kondo dot, Phys. Rev. Lett. **94**, 216601 (2005).

[46] A. O. Gogolin and A. Komnik, Towards full counting statistics for the Anderson impurity model, Phys. Rev. B **73**, 195301 (2006).

[47] M. Grobis, I. G. Rau, R. M. Potok, H. Shtrikman, and D. Goldhaber-Gordon, Universal scaling in nonequilibrium transport through a single channel Kondo dot, Phys. Rev. Lett. **100**, 246601 (2008).

[48] T. K. T. Nguyen and M. N. Kiselev, Thermoelectric transport in a three-channel charge Kondo circuit, Phys. Rev. Lett. **125**, 026801 (2020).

[49] X. Zheng, J. Jin, S. Welack, M. Luo, and Y. Yan, Numerical approach to time-dependent quantum transport and dynamical Kondo transition, J. Chem. Phys. **130**, 164708 (2009).

[50] M. Schiro and O. Scarlatella, Quantum impurity models coupled to Markovian and non-Markovian baths, J. Chem. Phys. **151**, 044102 (2019).

[51] G.-M. Tang and J. Wang, Full-counting statistics of charge and spin transport in the transient regime: A nonequilibrium Green's function approach, Phys. Rev. B **90**, 195422 (2014).

[52] T. Brandes, Waiting times and noise in single particle transport, Ann. Phys. (Berlin) **520**, 477 (2008).
[53] S. Welack, M. Esposito, U. Harbola, and S. Mukamel, Interference effects in the counting statistics of electron transfers through a double quantum dot, Phys. Rev. B **77**, 195315 (2008).
[54] S. Welack, S. Mukamel, and Y. Yan, Waiting time distributions of electron transfers through quantum dot Aharonov-Bohm interferometers, Europhys. Lett. **85**, 57008 (2009).
[55] S. Welack and Y. Yan, Non-Markovian theory for the waiting time distributions of single electron transfers, J. Chem. Phys. **131**, 114111 (2009).
[56] K. H. Thomas and C. Flindt, Electron waiting times in non-Markovian quantum transport, Phys. Rev. B **87**, 121405(R) (2013).
[57] G.-M. Tang, F. Xu, and J. Wang, Waiting time distribution of quantum electronic transport in the transient regime, Phys. Rev. B **89**, 205310 (2014).
[58] B. Sothmann, Electronic waiting-time distribution of a quantum-dot spin valve, Phys. Rev. B **90**, 155315 (2014).
[59] V. Talbo, J. Mateos, S. Retailleau, P. Dollfus, and T. González, Time-dependent shot noise in multi-level quantum dot-based single-electron devices, Semicond. Sci. Technol. **30**, 055002 (2015).
[60] S. L. Rudge and D. S. Kosov, Distribution of residence times as a marker to distinguish different pathways for quantum transport, Phys. Rev. E **94**, 042134 (2016).
[61] S. L. Rudge and D. S. Kosov, Distribution of tunnelling times for quantum electron transport, J. Chem. Phys. **144**, 124105 (2016).
[62] K. Ptaszyński, Nonrenewal statistics in transport through quantum dots, Phys. Rev. B **95**, 045306 (2017).
[63] S. L. Rudge and D. S. Kosov, Distribution of waiting times between electron cotunneling events, Phys. Rev. B **98**, 245402 (2018).
[64] P. Stegmann, J. König, and S. Weiss, Coherent dynamics in stochastic systems revealed by full counting statistics, Phys. Rev. B **98**, 035409 (2018).
[65] E. Kleinherbers, P. Stegmann, and J. König, Revealing attractive electron–electron interaction in a quantum dot by full counting statistics, New J. Phys. **20**, 073023 (2018).
[66] G. Tang, F. Xu, S. Mi, and J. Wang, Spin-resolved electron waiting times in a quantum-dot spin valve, Phys. Rev. B **97**, 165407 (2018).
[67] S. L. Rudge and D. S. Kosov, Nonrenewal statistics in quantum transport from the perspective of first-passage and waiting time distributions, Phys. Rev. B **99**, 115426 (2019).
[68] E. Kleinherbers, P. Stegmann, and J. König, Synchronized coherent charge oscillations in coupled double quantum dots, Phys. Rev. B **104**, 165304 (2021).
[69] P. Stegmann, B. Sothmann, J. König, and C. Flindt, Electron waiting times in a strongly interacting quantum dot: Interaction effects and higher-order tunneling processes, Phys. Rev. Lett. **127**, 096803 (2021).
[70] M. Albert, C. Flindt, and M. Büttiker, Distributions of waiting times of dynamic single-electron emitters, Phys. Rev. Lett. **107**, 086805 (2011).
[71] S. K. Gorman, Y. He, M. G. House, J. G. Keizer, D. Keith, L. Fricke, S. J. Hile, M. A. Broome, and M. Y. Simmons, Tunneling statistics for analysis of spin-readout fidelity, Phys. Rev. Appl. **8**, 034019 (2017).
[72] M. Jenei, E. Potanina, R. Zhao, K. Y. Tan, A. Rossi, T. Tanttu, K. W. Chan, V. Sevriuk, M. Möttönen, and A. Dzurak, Waiting time distributions in a two-level fluctuator coupled to a superconducting charge detector, Phys. Rev. Res. **1**, 033163 (2019).
[73] F. Brange, A. Schmidt, J. C. Bayer, T. Wagner, C. Flindt, and R. J. Haug, Controlled emission time statistics of a dynamic single-electron transistor, Sci. Adv. **7**, eabe0793 (2021).
[74] A. Ranni, F. Brange, E. T. Mannila, C. Flindt, and V. F. Maisi, Real-time observation of Cooper pair splitting showing strong non-local correlations, Nat. Commun. **12**, 6358 (2021).
[75] W. Fu, S.-S. Ke, Y. Guo, H.-W. Zhang, and H.-F. Lü, Waiting time distribution and current correlations via a Majorana single-charge transistor, Phys. Rev. B **106**, 075404 (2022).
[76] E. Kleinherbers, A. Schünemann, and J. König, Full counting statistics in a Majorana single-charge transistor, Phys. Rev. B **107**, 195407 (2023).
[77] J. C. Bayer, F. Brange, A. Schmidt, T. Wagner, E. P. Rugeramigabo, C. Flindt, and R. J. Haug, Real-time detection and control of correlated charge tunneling in a quantum dot, Phys. Rev. Lett. **134**, 046303 (2025).
[78] J. Hu, M. Luo, F. Jiang, R.-X. Xu, and Y. Yan, Padé spectrum decompositions of quantum distribution functions and optimal hierarchical equations of motion construction for quantum open systems, J. Chem. Phys. **134**, 244106 (2011).
[79] Y.-T. Huang, P.-C. Kuo, N. Lambert, M. Cirio, S. Cross, S.-L. Yang, F. Nori, and Y.-N. Chen, An efficient Julia framework for hierarchical equations of motion in open quantum systems, Commun. Phys. **6**, 313 (2023).
[80] Z. H. Li, N. H. Tong, X. Zheng, D. Hou, J. H. Wei, J. Hu, and Y. J. Yan, Hierarchical Liouville-space approach for accurate and universal characterization of quantum impurity systems, Phys. Rev. Lett. **109**, 266403 (2012).
[81] N. Lambert, T. Raheja, S. Cross, P. Menczel, S. Ahmed, A. Pitchford, D. Burgarth, and F. Nori, QuTiP-BoFiN: A bosonic and fermionic numerical hierarchical-equations-of-motion library with applications in light-harvesting, quantum control, and single-molecule electronics, Phys. Rev. Res. **5**, 013181 (2023).
[82] Y. Tanimura, Numerically "exact" approach to open quantum dynamics: The hierarchical equations of motion (HEOM), J. Chem. Phys **153**, 020901 (2020).
[83] M. Cirio, N. Lambert, P. Liang, P.-C. Kuo, Y.-N. Chen, P. Menczel, K. Funo, and F. Nori, Pseudofermion method for the exact description of fermionic environments: From single-molecule electronics to the Kondo resonance, Phys. Rev. Res. **5**, 033011 (2023).
[84] J.-D. Lin, P.-C. Kuo, N. Lambert, A. Miranowicz, F. Nori, and Y.-N. Chen, Non-Markovian quantum exceptional points, Nat. Commun. **16**, 1289 (2025).
[85] F. Beaudoin, J. M. Gambetta, and A. Blais, Dissipation and ultrastrong coupling in circuit QED, Phys. Rev. A **84**, 043832 (2011).
[86] L. Rajabi, C. Pöltl, and M. Governale, Waiting time distributions for the transport through a quantum-dot tunnel coupled

to one normal and one superconducting lead, Phys. Rev. Lett. **111**, 067002 (2013).

[87] K. Wrześniewski and I. Weymann, Current cross-correlations and waiting time distributions in Andreev transport through Cooper pair splitters based on a triple quantum dot system, Phys. Rev. B **101**, 155409 (2020).

[88] N. Roch, S. Florens, T. A. Costi, W. Wernsdorfer, and F. Balestro, Observation of the underscreened Kondo effect in a molecular transistor, Phys. Rev. Lett. **103**, 197202 (2009).

[89] M. Cirio, P. C. Kuo, Y. N. Chen, F. Nori, and N. Lambert, Canonical derivation of the fermionic influence superoperator, Phys. Rev. B **105**, 035121 (2022).

[90] T. A. Costi, Kondo effect in a magnetic field and the magnetoresistivity of Kondo alloys, Phys. Rev. Lett. **85**, 1504 (2000).

[91] W. Liang, M. P. Shores, M. Bockrath, J. R. Long, and H. Park, Kondo resonance in a single-molecule transistor, Nature (London) **417**, 725 (2002).

[92] Y.-h. Zhang, S. Kahle, T. Herden, C. Stroh, M. Mayor, U. Schlickum, M. Ternes, P. Wahl, and K. Kern, Temperature and magnetic field dependence of a Kondo system in the weak coupling regime, Nat. Commun. **4**, 2110 (2013).

[93] K. Nagaoka, T. Jamneala, M. Grobis, and M. F. Crommie, Temperature dependence of a single Kondo impurity, Phys. Rev. Lett. **88**, 077205 (2002).

[94] Y. Cheng, W. Hou, Y. Wang, Z. Li, J. Wei, and Y. Yan, Time-dependent transport through quantum-impurity systems with Kondo resonance, New J. Phys. **17**, 033009 (2015).

[95] H. Shiono, S. Ishihara, K. Mimura, H. Sato, E. F. Schwier, K. Shimada, M. Taniguchi, S.-i. Ideta, K. Tanaka, T. Zhuang, K. T. Matsumoto, K. Hiraoka, and H. Anzai, Temperature dependence of the Kondo resonance peak in photoemission spectra of $YbCdCu_4$, AIP Conf. Proc. **2054**, 040013 (2019).

[96] M.-T. Tran and T. T. Nguyen, Molecular Kondo effect in flat-band lattices, Phys. Rev. B **97**, 155125 (2018).

[97] R. Allub and C. R. Proetto, Anderson model out of equilibrium: Zero-bandwidth limit, Phys. Rev. B **62**, 10923 (2000).

[98] G. Cohen and E. Rabani, Memory effects in nonequilibrium quantum impurity models, Phys. Rev. B **84**, 075150 (2011).

[99] V. Bruch, M. Pletyukhov, H. Schoeller, and D. M. Kennes, Floquet renormalization group approach to the periodically driven Kondo model, Phys. Rev. B **106**, 115440 (2022).

[100] L. Cao, L. Ge, D. Zhang, X. Li, Y. Wang, R.-X. Xu, Y. Yan, and X. Zheng, Simulating non-Markovian open quantum dynamics with neural quantum states, arXiv:2404.11093v2.

[101] M. Vanhoecke and M. Schirò, Kondo-Zeno crossover in the dynamics of a monitored quantum dot, Nat. Commun. **16**, 6155 (2025).

[102] F. Brange, P. Menczel, and C. Flindt, Photon counting statistics of a microwave cavity, Phys. Rev. B **99**, 085418 (2019).

[103] C. Schinabeck and M. Thoss, Hierarchical quantum master equation approach to current fluctuations in nonequilibrium charge transport through nanosystems, Phys. Rev. B **101**, 075422 (2020).

[104] S. A. Gurvitz, Rate equations for quantum transport in multi-dot systems, Phys. Rev. B **57**, 6602 (1998).

[105] X. Dan, M. Xu, J. T. Stockburger, J. Ankerhold, and Q. Shi, Efficient low-temperature simulations for fermionic reservoirs with the hierarchical equations of motion method: Application to the Anderson impurity model, Phys. Rev. B **107**, 195429 (2023).